Chapter 6

Envelope structure of deeply embedded young stellar objects in the Serpens Molecular Cloud

Abstract

The structure of the envelopes surrounding deeply embedded young stellar objects (SMM 1 = FIRS 1, SMM 2, SMM 3, SMM 4) located in the Serpens Molecular Cloud is investigated through aperture-synthesis and single-dish observations of molecular lines and continuum emission at (sub)millimeter wavelengths. SMM 1, 3, and 4 show partially resolved ($> 2'' = 800$ AU) continuum emission in the beam of the Owens Valley Millimeter Array at $\lambda = 3.4$–1.4 mm. The continuum visibilities accurately constrain the density structure in the envelopes, which can be described by a radial power law with slope -2.0 ± 0.5 on scales of 300 AU to 8000 AU. Inferred envelope masses are 8.7, 3.0, and 5.3 $M_\odot$ for SMM 1, 3, and 4, respectively. A point source with 20%–30% of the total flux at 1.1 mm is required to fit the observations on long baselines, corresponding to warm envelope material within $\sim$ 100 AU or a circumstellar disk. No continuum emission is detected interferometrically toward SMM 2, corresponding to an upper limit of 0.2 $M_\odot$ assuming $T_{\rm d} = 24$ K. The lack of any compact dust emission suggests that the SMM 2 core does not contain a central protostar.

Aperture-synthesis observations of ^{13}CO, C^{18}O, HCO$^+$, H^{13}CO$^+$, HCN, H^{13}CN, and N_2H^+ J=1–0, and SiO 2–1 and SO 2_2-1_1, reveal compact emission toward SMM 1, 3, and 4. SMM 2 shows only a number of clumps scattered throughout the primary field of view, supporting the conclusion that this core does not contain a central star. The compact molecular emission around SMM 1, 3, and 4 traces $5''$–$10''$ (2000–4000 AU) diameter cores around the sources corresponding to the densest regions of the envelopes, as well as material directly associated with the molecular outflow. Especially prominent are the optically thick HCN and HCO$^+$ lines which show up brightly along the walls of the outflow cavities. SO and SiO trace shocked material and may have enhanced abundances of a few times 10^{-8} and a few times 10^{-7} with respect to H_2.

A total of 31 molecular transitions have been observed with the James Clerk Maxwell and Caltech Submillimeter telescopes in the 230, 345, 490, and 690 GHz atmospheric windows toward all four sources, containing lines of CO, HCO$^+$, HCN, H_2CO, SiO, SO, and their isotopomers. These lines show 20–30 km s^{-1} wide line wings, deep and narrow (1–2 km s^{-1}) self-absorption, and 2–3 km s^{-1} FWHM line cores. The presence of highly excited lines like ^{12}CO 4–3 and 6–5, ^{13}CO

Hogerheijde, van Dishoeck, Salverda, & Blake 1998b, submitted to ApJ

6–5, and several H_2CO transitions indicates the presence of material with temperatures $\gtrsim$100 K. Monte Carlo calculations of the molecular excitation and line transfer show that the envelope model derived from the dust emission can successfully reproduce the observed single-dish and interferometric line intensities, if an additional column of $\sim$ 100 K material is included to reproduce the highly excited lines of CO and H_2CO. This component contains less than 1% of the total envelope mass, and may be associated with the outflow. The model fits imply average abundances of (1–5)$\times 10^{-9}$ for HCO^+ and HCN, and 1×10^{-9}–3×10^{-8} for H_2CO for the four sources, with H_2CO probably enhanced in the warm central regions of the envelope. Taken together, the observations presented in this chapter give a detailed picture of the envelope structure on scales between 1000 and 10,000 AU.

6.1 Introduction

The earliest stages of star formation are represented by deeply embedded, class 0 young stellar objects (YSOs; André, Ward-Thompson, & Barsony 1993). These sources have spectral energy distributions (SEDs) which are well fit by a single black body curve of $T_{\rm eff} \lesssim$ 30 K, are undetected at wavelengths shorter than $\sim$ 10 μm, and still have most of their mass in a circumstellar envelope. Thus, class 0 sources are ideal objects to investigate the physical and chemical conditions during the earliest phases of the star-forming process, to test theoretical models of cloud core collapse (e.g., Shu 1977; Terebey, Shu, & Cassen 1984; Fiedler & Mouschovias 1992; Boss 1993), and to study the influence of the bipolar outflow on the structure and chemistry of the envelope. This chapter presents single-dish and aperture synthesis observations of dust and molecular lines of four class 0 candidates in the Serpens Molecular Cloud, tracing the structure and chemistry of their envelopes on 1000–10,000 AU scales ($3''$–$30''$).

Recently, dust continuum and molecular line observations have begun to probe the structure and chemistry of the envelopes surrounding a number of class 0 YSOs (e.g., NGC 1333 IRAS 4A and 4B, Blake et al. 1995; IRAS 16293−2422, Walker, Carlstrom, & Bieging 1993; Blake et al. 1994, van Dishoeck et al. 1995). These observations show that the envelopes are dense, with $n_{\rm H_2} \approx 10^6$–10^7 cm^{-3}, and cold, at $T_{\rm d} \approx 30$ K, and that the molecular abundances may be significantly depleted by freezing out onto dust grains (e.g, Blake et al. 1995; see also Mundy & McMullin 1997). Surveys in HCO^+ (Gregersen et al. 1997), and in H_2CO, CS, and N_2H^+ (Mardones et al. 1997) indicate that line-profile asymmetries predicted for infalling envelopes are more readily observed during the deeply embedded class 0 phase than toward more evolved class I objects. Also, class 0 YSOs are often found to drive highly collimated outflows (e.g., André et al. 1990; Guilloteau et al. 1992; Zhang et al. 1995; Blake et al. 1995; Gueth et al. 1997). These outflows affect the structure of the molecular envelope, as well as its chemistry, through shocks and by heating a small fraction of the gas to 60 K or more, thus releasing molecules from grain surfaces into the gas phase (e.g., van Dishoeck et al. 1995; Blake et al. 1995; Bachiller & Pérez Gutiérrez 1997). Important, unanswered questions about the envelopes around class 0 sources are how their density structure compares to theoretical models of protostellar collapse, to what extent their structure and chemistry on 1000 AU scales is influenced by the outflow, and how strongly molecular abundances are depleted in the cold, dense regions.

The Serpens Molecular Cloud appears to be forming a loosely bound cluster of low- to intermediate-mass stars. Eiroa & Casali (1992) have identified 51 near-infrared sources as T Tauri stars (see also Giovannetti et al. 1998). Casali, Eiroa, & Duncan (1993) have detected four submillimeter continuum sources without any near-infrared counterparts (SMM 1, 2, 3, and 4). These objects represent a second, more recent phase of star formation in the Serpens cloud. Their spectral energy distributions are well fit by single blackbodies with temperatures of 20–27 K, characteristic of class 0 YSOs (Hurt & Barsony 1996a). Observations of ^{12}CO, HCO$^+$, and H_2CO lines indicate the presence of warm ($T_{\rm kin}$ = 40–190 K) and dense ($n_{\rm H_2} \approx 2\times10^6$ cm^{-3}) gas associated with bipolar outflows, as evidenced by broad line wings (White, Casali, & Eiroa 1995; Hurt, Barsony, & Wootten 1996b). Herbst, Beckwith, & Robberto (1997a) detected a number of H_2 knots, possibly a jet, emanating from SMM 3, whereas Eiroa et al. (1997) report the detection of a similar string of H_2 knots, possibly associated with SMM 4. Nordh et al. (1982) and Harvey et al. (1984) already identified SMM 1, also called FIRS 1, as a deeply embedded YSO. It shows several signs of energetic activity, such as H_2O maser emission (Dinger & Dickinson 1980; Rodríguez et al. 1980) and near-infrared H_2 emission (Eiroa & Casali 1989). At cm wavelengths, the source is triple, with two diametrically opposed lobes moving away at $\sim$ 200 km s^{-1} from the central source. McMullin et al. (1994) performed an interferometric and single-dish study of SMM 1 and the condensation S68 N, 2$'$ north of SMM 1, using lines of CS, CH_3OH, and other molecules. They find that most of the 70 $M_\odot$ in this northwestern condensation is distributed on extended scales, indicative of a young age of the sources, with $\sim$ 10 $M_\odot$ in a circumstellar component around SMM 1. They infer abundances for CO and HCO$^+$ corresponding to those found in dark clouds, while CS, HCN, and H_2CO may be mildly depleted.

The distance to the Serpens cloud core has been the subject of much debate. De Lara, Chavarria-K, & López-Molina (1991) derive a value of 310 ± 40 pc, based on extinction measurement of five stars. Chiar (1996) and Chiar & Whittet (1998) find 425 ± 45 pc based on seven stars, including new observations of the five stars used by de Lara et al., all of which indicate a larger distance. One of these stars, R16, has a derived distance of 628 pc, but is included by Chiar & Whittet because its image on the POSS plate suggests it is an embedded object associated with the Serpens cloud. Excluding this star lowers the distance estimate to 390 pc. Here we will adopt 400 pc as a fiducial estimate of the distance to Serpens. Bolometric luminosities and other quantities taken from the literature are scaled to the adopted distance.

In this chapter, we present single-dish and aperture-synthesis observations of molecular lines and dust continuum at (sub)millimeter wavelengths toward SMM 1, 2, 3, and 4, with spatial resolutions between 1$''$ and 20$''$ ($\sim$ 400–8000 AU). The protostellar nature of three sources, SMM 1, 3, and 4, is confirmed on the basis of the interferometer results, while SMM 2 appears to be a warm cloud condensation without any central source. The continuum observations allow a determination of the density and temperature structure of the envelopes surrounding SMM 1, 3, and 4. The molecular line data can be explained by this same envelope model, but require that $\sim$ 1% of the gas has a

Table 6.1. Source sample

Source	$\alpha_{1950.0}$[a] (h m s)	$\delta_{1950.0}$[a] (° ′ ″)	$L_{\rm bol}$[b] ($L_\odot$)	F_ν (1.1 mm) (Jy)	$M_\star$[c] ($M_\odot$)
SMM 1 = FIRS 1	18 27 17.3	+01 13 16	77	3.47 ± 0.1	0.7–3.9
SMM 2	18 27 28.0[d]	+01 10 45[d]	10	0.6 ± 0.1	0.1–2.1
SMM 3	18 27 26.9	+01 11 55	13	1.11 ± 0.1	0.1–2.2
SMM 4	18 27 24.3	+01 11 10	15	1.47 ± 0.1	0.1–2.3

[a] Best-fit positions to continuum interferometric data (see §6.3.1).

[b] Scaled to a distance of 400 pc.

[c] Constraints on stellar mass derived from bolometric luminosity. Lower limit: $L_{\rm bol}$ due to accretion at $\dot{M} = 10^{-5}$ $M_\odot$ yr^{-1} onto star with 3 $R_\odot$ radius. Upper limit: main-sequence mass of star with stellar luminosity equal to $L_{\rm bol}$.

[d] No continuum emission detected in interferometer beam. Submillimeter position of Casali et al. (1993) is given.

References: Casali et al. 1993 (F_ν 1.1 mm); Hurt & Barsony 1996 ($L_{\rm bol}$).

much higher temperature of $\sim$ 100 K. The aperture-synthesis observations trace 5″–10″ (2000–4000 AU) cores around the YSOs, as well as the interaction of the outflow with surrounding material. This study of a group of deeply embedded YSOs has the spatial resolution of a few arcseconds required to directly sample the protostellar envelopes, and the Serpens results will be compared to class 0 objects in other clouds, as well as to a set of more evolved class I sources studied in the same molecular lines in Chapters 2 and 3 (Hogerheijde et al. 1997a, 1998a).

The outline of the chapter is as follows. After presenting the details of the observations in §6.2, we discuss the results of the continuum measurements in §6.3.1, and construct an envelope model in §6.3.2. Section 6.4 analyzes in detail the molecular line emission observed in the interferometer (§6.4.1) and single-dish beams (§6.4.2) toward the individual sources. In §6.4.3 the molecular line emission is compared to model predictions based on the envelope structure derived from the dust continuum. The results are further discussed and compared to other class 0 and class I YSOs in §6.5. Section 6.6 finally summarizes the main findings of the chapter.

6.2 Observations

The coordinates of SMM 1, 2, 3, and 4 are listed in Table 6.1, together with their bolometric luminosity scaled to a distance of 400 pc, continuum flux at $\lambda = 1.1$ mm, and estimates of the stellar mass. The coordinates are derived from the interferometric continuum emission, and differ by up to 5″ from those quoted by Casali et al. (1993) for SMM 3 and 4. Lower limits to the stellar masses follow from the assumption that all luminosity is due to accretion at a rate of 10^{-5} $M_\odot$ yr^{-1}, while upper limits are the stellar masses which produce the same luminosity on the zero-age main sequence. An overview of the data presented in this chapter is given in Table 6.2. The following subsections present the details of the interferometer and single-dish observations.

6.2.1 Millimeter-interferometer observations

Observations of the transitions listed in Table 6.2 were obtained with the six-element Owens Valley Radio Observatory (OVRO) Millimeter Array[1] between 1994 and 1997, simultaneously with the continuum emission over a 1 GHz bandwidth at $\lambda = 3.4$, 3.2, 2.7, and 1.4 mm. Data taken in the low-resolution and equatorial configurations were combined, resulting in a *u-v* coverage with spacings between 3 and 60–80 kλ at 3.4–2.7 mm, for the observed lines and continuum, and between 10 and 100–180 kλ at 1.4 mm in continuum only. This corresponds to naturally weighted, synthesized beams of $3''$–$5''$ and $1''$ FWHM, respectively. Spectral line data were recorded in two 64-channel bands with respective widths of 2 and 8 MHz, resulting in velocity resolutions of ~ 0.1 and ~ 0.4 km s^{-1}. The visibility data were calibrated using the MMA package, developed specifically for OVRO (Scoville et al. 1993). The quasar PKS 1749+096 served as phase calibrator; the amplitudes were calibrated on 3C 454.3, 3C 273, or Neptune. The correlator passbands are calibrated using noise tube integrations and observations of 3C 454.3 and 3C 273.

The interferometer data were edited in the usual manner by flagging a small number of data points with clearly deviating amplitudes and phases. The quality of the continuum data at 3.4–2.7 mm allowed self-calibration of the visibility phases, which was subsequently applied to the line data, decreasing the noise level by a small amount. Natural weighting was used to clean the data. The interferometer dirty beam has strong north–south side lobes because of the low declination of Serpens of $+1°$. In many cases the position of the initial clean-components had to be constrained to a $\sim 20''$ box around the source position to ensure proper deconvolution. An additional complication for cleaning of the molecular-line data toward SMM 3 was the presence of strong emission from SMM 4 approximately one primary beam ($\sim 70''$) to the south. Care had to be taken to prevent any emission from SMM 4 appearing within the primary field of view around SMM 3.

The reduced continuum data have RMS noise levels of 2–6 mJy beam^{-1} at 3.4–2.7 mm and 30 mJy beam^{-1} at 1.4 mm. For the molecular line data the typical noise is 0.1–0.2 Jy beam^{-1} per 125 kHz channel. Reduction and analysis of the visibility data were carried out within the MIRIAD software package.

6.2.2 Single-dish observations

The single-dish line observations between 219 and 690 GHz were obtained between 1995 March and 1996 August with the James Clerk Maxwell Telescope (JCMT)[2] and

---

[1] The Owens Valley Millimeter Array is operated by the California Institute of Technology under funding from the U.S. National Science Foundation (#AST96–13717).

[2] The James Clerk Maxwell Telescope is operated by the Joint Astronomy Centre, on behalf of the Particle Physics and Astronomy Research Council of the United Kingdom, the Netherlands Organization for Scientific Research and the National Research Council of Canada.

Table 6.2. Overview of observations

Date	Instrument	Observation
	Interferometer data	
1994 Oct–Dec, 1996 Feb–May, 1997 Feb–Apr	OVRO	$F_\nu(\lambda = 3.4$ mm)
1997 Apr	OVRO	$F_\nu(\lambda = 3.2$ mm)[a]
1995 Feb, May, 1997 Feb–Mar	OVRO	$F_\nu(\lambda = 2.7$ mm)
1997 Feb–Mar	OVRO	$F_\nu(\lambda = 1.3$ mm)[b]
1997 Apr	OVRO	$F_\nu(\lambda = 1.4$ mm)[a]
1995 Feb, May, 1997 Feb–Apr	OVRO	^{13}CO 1–0; C^{18}O 1–0
1994 Oct–Dec	OVRO	HCO$^+$ 1–0; H^{13}CO$^+$ 1–0; SiO 2–1
1996 Feb–May, 1997 Feb–Apr	OVRO	HCN 1–0; H^{13}CN 1–0; C_3H_2 4_{32}–4_{23}; SO 2_2–1_1
1997 Apr	OVRO	N_2H^+ 1–0[a]; C^{34}S 2–1[a]
	Single-dish data	
1995 May	CSO	^{12}CO 6–5[d]; ^{13}CO 6–5[d]
1995 Oct	CSO	H^{13}CO$^+$ 4–3; SO 8_8–7_7
1995 Mar, Jun	JCMT	^{12}CO 4–3[e]; ^{13}CO 2–1, 3–2; C^{18}O 2–1; C^{17}O 3–2; SiO 6–5; HCO$^+$ 3–2[e], 4–3[e]; H^{13}CO$^+$ 3–2[f]; HC_3N 24–23[f]; SO 5_5–4_4[f,g]; CN 3–1, 5–3, 7–5, 3–3, 5–5[h]; H_2CO 7_{17}–6_{16}, 5_{15}–4_{14}, 5_{33}–4_{32}[c], 5_{32}–4_{31}[c], 3_{03}–2_{02}[f], 3_{22}–2_{21}[f,g]; C_3H_2 5_{24}–4_{13}[f], 5_{32}–4_{41}; CH_3OH 4_2–3_1 E[f]; C I $^3P_1$–$^3P_0$
1996 Aug	JCMT	HCN 4–3; H^{13}CN 4–3

[a] SMM 1 and SMM 4 only.
[b] SMM 2 and SMM 3 only.
[c] SMM 1 only.
[d] Five-point map obtained.
[e] Map obtained.
[f] Map obtained of SMM 1 only.
[g] H_2CO 3_{22}–2_{21} and SO 5_5–4_4 are partially blended, in upper and lower sideband respectively.
[h] CN $3\frac{5}{2}\frac{u}{2}$–$2\frac{3}{2}\frac{l}{2}$; u and l are indicated in the table.

the Caltech Submillimeter Observatory (CSO)[3] . The observed transitions are listed in Table 6.2. The single-dish observations were reduced and analyzed with the CLASS software package.

The JCMT observations in the 230, 345, and 490 GHz atmospheric windows were obtained with FWHM beam sizes of 19″, 14″, and 10″, respectively. The observations were made using a position-switch of typically 15′–60′, ensuring emission-free offset positions. Pointing accuracy is estimated to be $\sim 5''$. In a number of lines, as indi-

[3] The Caltech Submillimeter Observatory is operated by the California Institute of Technology under funding from the U.S. National Science Foundation (#AST96–15025).

cated in Table 6.2, maps covering regions between 20″ × 20″ and 40″ × 40″ around the sources were taken, sampled at $\frac{1}{2}$–$\frac{2}{3}$ beam sizes. In HCO^+ 3–2, fully sampled maps were obtained *on-the-fly*. The spectra were recorded with the Digital Autocorrelation Spectrometer, with typical velocity resolutions of 0.05–0.1 km s^{-1}. The H_2CO 3_{03}–2_{02} and 3_{22}–2_{21} spectra were observed in a single frequency setting over a total bandwidth of 500 MHz and at a resolution of 0.9 km s^{-1}, also covering the HC_3N 24–23, C_3H_2 5_{24}–4_{13}, CH_3OH 4_2–3_1 E, and SO 5_5–4_4 lines. The data were converted to the main-beam antenna temperature scale using $\eta_{\rm mb} = 0.69$ (230 GHz), 0.58 (345 GHz), and 0.53 (490 GHz), obtained by the JCMT staff from measurements of the planets. Typical RMS noise levels are 0.1–0.3 K in 0.15 km s^{-1} wide channels.

Using the CSO, observations were obtained of ^{12}CO and ^{13}CO 6–5 with a FWHM beam size of 10″, and of $H^{13}CO^+$ 4–3 at 22″, the latter of which also contains the SO 8_8-7_7 line. The observations were made using a position switch of 15′ for the ^{12}CO and ^{13}CO spectra, and a beam switch of 180″ for the $H^{13}CO^+$ data, ensuring emission-free offset positions. Pointing was checked regularly, and found to vary by up to 5″. At the frequency of the ^{12}CO and ^{13}CO 6–5 lines (660–690 GHz), an additional source of positional error was the correction for the atmospheric diffraction, which is comparable to the FWHM beam size ($\sim$ 10″). It is estimated that the pointing at these frequencies is no better than $\sim$ 10″. Five-point maps with 10″ spacing were obtained for ^{12}CO and ^{13}CO 6–5. The spectral lines were recorded with the facility 50 MHz and 500 MHz bandwidth Acousto–Optical Spectrometers (AOSs). The spectra were converted to the main-beam antenna scale using $\eta_{\rm mb}$ = 0.44 (^{12}CO, ^{13}CO) and 0.65 ($H^{13}CO^+$, SO), obtained from measurements of Jupiter. Resulting RMS noise levels are 0.6 K per 0.5 km s^{-1} channel for ^{12}CO and ^{13}CO, and 0.1 K per 0.15 km s^{-1} for $H^{13}CO^+$ and SO.

6.3 Dust continuum emission

6.3.1 Interferometer results

Continuum emission at λ = 3.4, 3.2, 2.7, and 1.4 mm is readily detected by OVRO toward SMM 1, 3, and 4. Peak intensities and integrated fluxes are listed in Table 6.3. No continuum emission is detected toward SMM 2 with an upper limit of $\sim$ 5 mJy at 3.4 mm. Figure 6.1 shows the naturally weighted, cleaned continuum images. The emission is mostly unresolved and symmetric about the source position. Table 6.1 lists the best-fit source positions for SMM 1, 3, and 4. Our observations, which have higher spatial resolution and positional accuracy than do the JCMT continuum maps of Casali et al. (1993), yield positions for SMM 3 and SMM 4 nearly 5″ west of those listed by these authors. We will adopt our best-fit coordinates as the true positions of SMM 3 and 4. The best-fit coordinates of SMM 1 agree with the radio position from Rodríguez et al. (1989) to within the accuracy of the measurements. Its emission at cm wavelengths, and the expected flat spectral index for non-thermal radiation, indicates that > 95% of the emission of SMM 1 at 3.4–1.4 mm is due to thermal emission from dust (Rodríguez et al. 1989; McMullin et al. 1994).

Figure 6.2 shows the vector-averaged visibility amplitudes as functions of projected baseline length for the observed sources and wavelengths, averaged in 5–10 kλ wide

Table 6.3. Millimeter-continuum data

source	λ (mm)	beam ($''$)	I(max) (Jy beam^{-1})	F_ν(total) (Jy)
SMM 1	3.4	5.8×4.9	0.126	0.202
	3.2	2.4×1.5	0.122	0.204
	2.7	3.2×2.7	0.183	0.414
	1.4	1.1×0.7	0.615	2.650
SMM 2	3.4	5.3×5.0	< 0.005	...
	2.7	4.2×3.6	< 0.008	...
	1.4	2.4×1.5	< 0.11	...
SMM 3	3.4	5.2×4.4	0.043	0.052
	2.7	4.3×3.6	0.090	0.104
	1.4	2.4×1.5	0.651	0.900
SMM 4	3.4	5.3×4.6	0.060	0.075
	3.2	2.6×1.5	0.068	0.097
	2.7	3.2×2.7	0.092	0.143
	1.4	1.1×0.7	0.462	1.108

bins. These plots essentially give the Fourier transform of the symmetric part of the sky brightness about the source center. A point source has a flux independent of baseline length, while the flux of an extended source decreases with increasing u-v separation. The observations show both extended and unresolved ($< 2'' = 800$ AU) emission towards SMM 1, 3, and 4. The extended emission traces the envelopes surrounding the sources, and the steep decrease of flux with u-v distance suggests a radial power-law distribution for the density. A Gaussian distribution, for example, would appear Gaussian as well in a plot of this type. The unresolved emission may contain contributions from the dense central regions of the power-law envelope as well as that from a circumstellar disk. The amplitudes on baselines $\gtrsim$60 kλ at the different wavelengths indicate a spectral index of 2.0 for the unresolved emission, consistent with optically thick, thermal emission.

6.3.2 A model for the continuum emission

The high signal-to-noise of the continuum data allows fitting of an envelope model to the 3.4–1.4 mm visibility data as well as the single-dish (sub)millimeter and IRAS fluxes given by Casali et al. (1993) and Hurt & Barsony (1996a), placing constraints on the mass and density distribution therein. Our modeling of the visibility data explicitly includes the sampling at discrete (u, v) positions, including the resolving out of emission on scales larger than those measured on the shortest baselines. For the density distribution we assume a radial power law, $\rho \propto r^{-p}$, with index p = 1.0–3.0. Theoretical models for cloud core collapse predict slopes between -1 and -2 (e.g., Shu 1977; Lizano & Shu 1989). The adopted temperature distribution is based on self-consistent modeling of the heating and cooling balance of the dust given a central luminosity of 50 $L_{\rm bol}$ and the dust emissivities as tabulated by Ossenkopf & Henning (1994). For the derived densities, the dust temperature is found to follow a power law with slope -0.4 for $r \gtrsim 450$ AU as expected for a cloud which is optically thin to the bulk of the

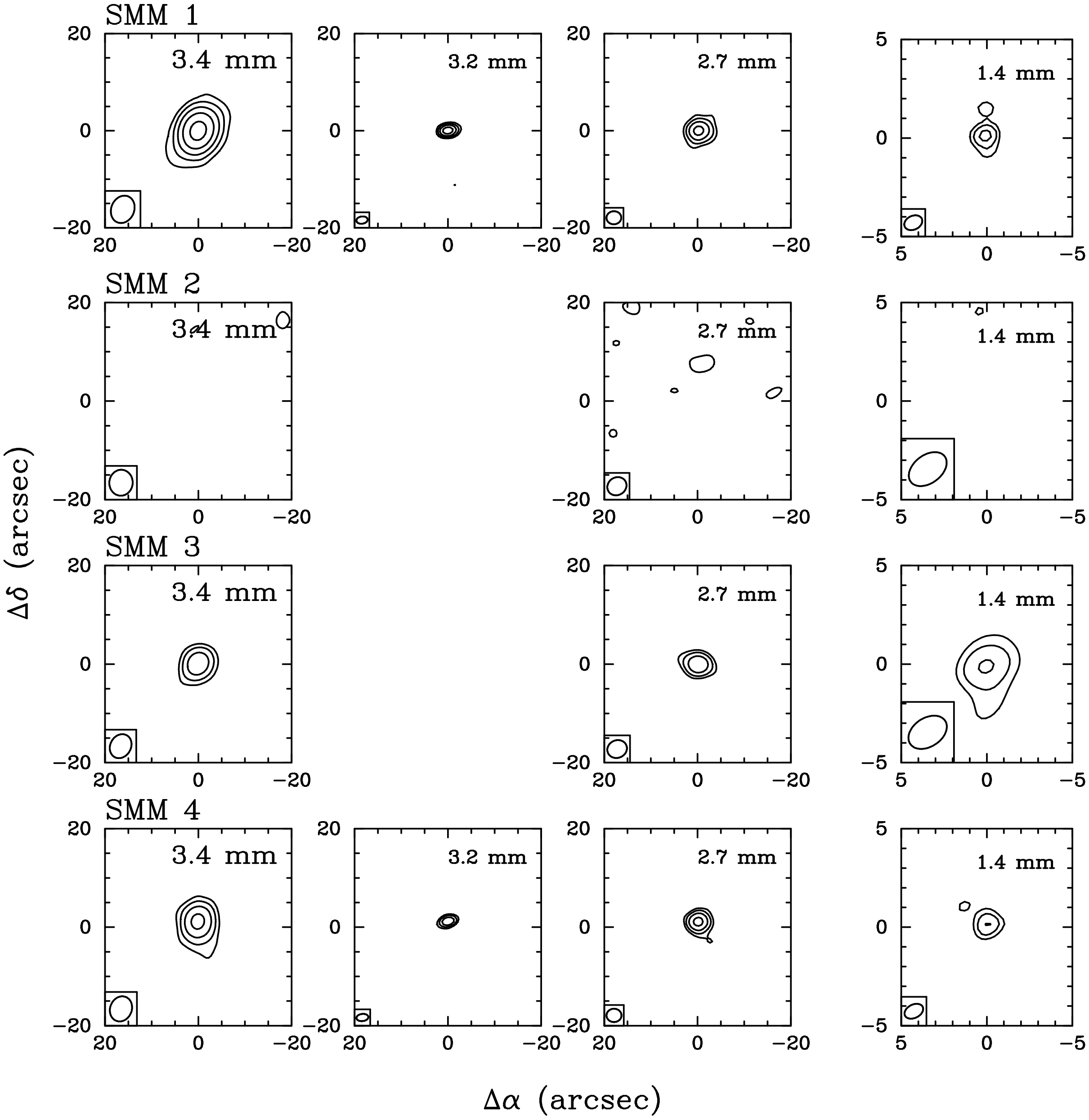

Fig. 6.1. *Cleaned, uniformly weighted images of continuum emission at* λ *=3.4, 3.2, 2.7, and 1.4 mm of SMM 1, 2, 3, and 4 observed with OVRO. Contour levels are drawn at 3*σ *intervals of 2–6 mJy beam*$^{-1}$ *at 3.4–2.7 mm and 16 mJy beam*$^{-1}$ *at 1.4 mm. Synthesized beam sizes are indicated in each panel. Note the much smaller depicted region at 1.4 mm.*

heating radiation (cf. Rowan-Robinson 1980; Adams & Shu 1987). The temperature is not allowed to drop below 8 K, corresponding to the typical value maintained through cosmic ray heating of the hydrogen gas. For $r < 450$ AU, the opacity causes the slope of the temperature distribution to increase, to roughly -0.9 at 100 AU (see van der Tak et al. 1998 for details of the temperature calculations). At radii smaller than 100 AU the density distribution can probably no longer be accurately described by our sim-

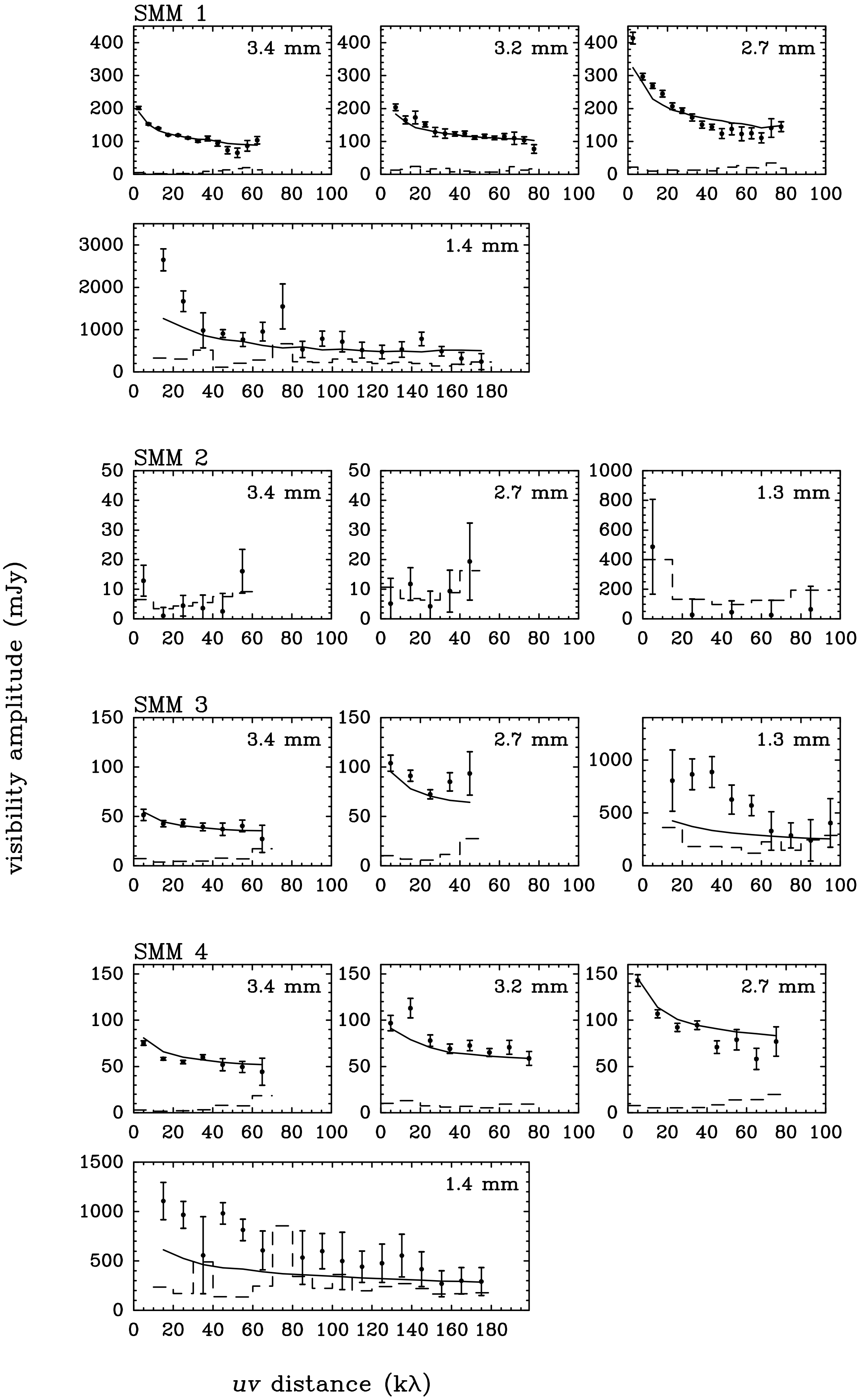
SMM 1
3.4 mm
3.2 mm
2.7 mm
1.4 mm
SMM 2
3.4 mm
2.7 mm
1.3 mm
SMM 3
3.4 mm
2.7 mm
1.3 mm
SMM 4
3.4 mm
3.2 mm
2.7 mm
1.4 mm
visibility amplitude (mJy)
uv distance (kλ)

Fig. 6.2. (Left) *Vector-averaged visibility amplitudes of observed continuum emission at 3.4, 3.2, 2.7 and 1.4 mm in mJy as a function of projected baseline length in kλ. The data are plotted as filled symbols, together with 1σ error bars. The dashed histogram shows the zero-signal expectation value. The solid lines are best-fit models as described in §6.3.2, for a density power-law slope of -2.0 and point source fluxes of §6.3.2. These model curves are not smooth because of incomplete sampling of the (u, v) plane in the original data set.*

ple spherically symmetric envelope model. Since our observations only constrain the density distribution at radii between 300 and 8000 AU which are actually resolved by our interferometer data, a much smaller value of 100 AU is adopted as the inner radius for the envelope model. All emission originating from within this radius is fitted separately by an additional point source, with a spectral index of $\alpha = 2.0$ (see §6.3.1). The adopted outer radius of 8000 AU does not affect the model results. Values for the dust emissivity at millimeter wavelengths are taken from Ossenkopf & Henning (1994), which includes dust coagulation in a medium of 10^6 H_2 cm^{-3} and thin ice mantles, with $\kappa_\nu(1.3 \text{ mm}) = 0.9$ cm^2 g^{-1}(dust) and $\kappa_\nu \propto \nu^{1.5}$.

To fit the peak of the SED at 50–100 μm, dust temperatures at 1000 AU of 27 K (SMM 1), 24 K (SMM 3), and 20 K (SMM 4) are required, similar to the values found by Hurt & Barsony (1996a). The latter authors assume a single dust temperature, but our derived temperature gradient is sufficiently shallow to give similar results. The total mass in the envelopes follows from the 1.1 mm continuum fluxes observed in the 18$''$ JCMT beam (Casali et al. 1993), and depends on the density power law index p and the flux of the additionally required point sources. The latter never exceed 30% of the total 1.1 mm fluxes.

The visibility amplitude as a function of u-v separation depends sensitively on the assumed density power-law index. Figure 6.3 shows the visibility amplitude against u-v separation for various power-law indices and point-source fluxes. Models with a shallower density distribution have amplitudes which decrease faster with increasing u-v distance. The calculations shown in the figure have been fitted to the total 1.1 mm flux of SMM 1, and sampled at the same (u, v) positions. The best correspondence to the observed amplitudes of SMM 1 is found for $p = 2.0 \pm 0.5$, which accurately fits the flux increase toward smaller u-v distances, and a point-source flux of 0.13 Jy at 2.7 mm, fitting the amplitude on long baselines. Similar best-fit results with $p = 2.0 \pm 0.5$ are found for SMM 3 and 4 with point-source fluxes at 2.7 mm of 0.05 Jy and 0.07 Jy, respectively. The corresponding curves are drawn in Fig. 6.2 for all sources. The inferred slopes of -2.0 for the density agree well with theoretical predictions for very young sources (e.g., Shu 1977). While the model curves provide very good fits to the 3.4–2.7 mm fluxes, they do underestimate the large scale emission at 1.4 mm. Part of this discrepancy may be explained by a steeper frequency dependency of the dust emissivity than the ~ 1.5 of the adopted model (Ossenkopf & Henning 1994). It may also indicate that warm material is distributed over larger scales than assumed in the model, in which it is confined to the inner few hundred AU.

The corresponding envelope masses, within an outer radius of 8000 AU, are 8.7 $M_\odot$ for SMM 1, 3.0 $M_\odot$ for SMM 3, and 5.3 $M_\odot$ for SMM 4. These values depend

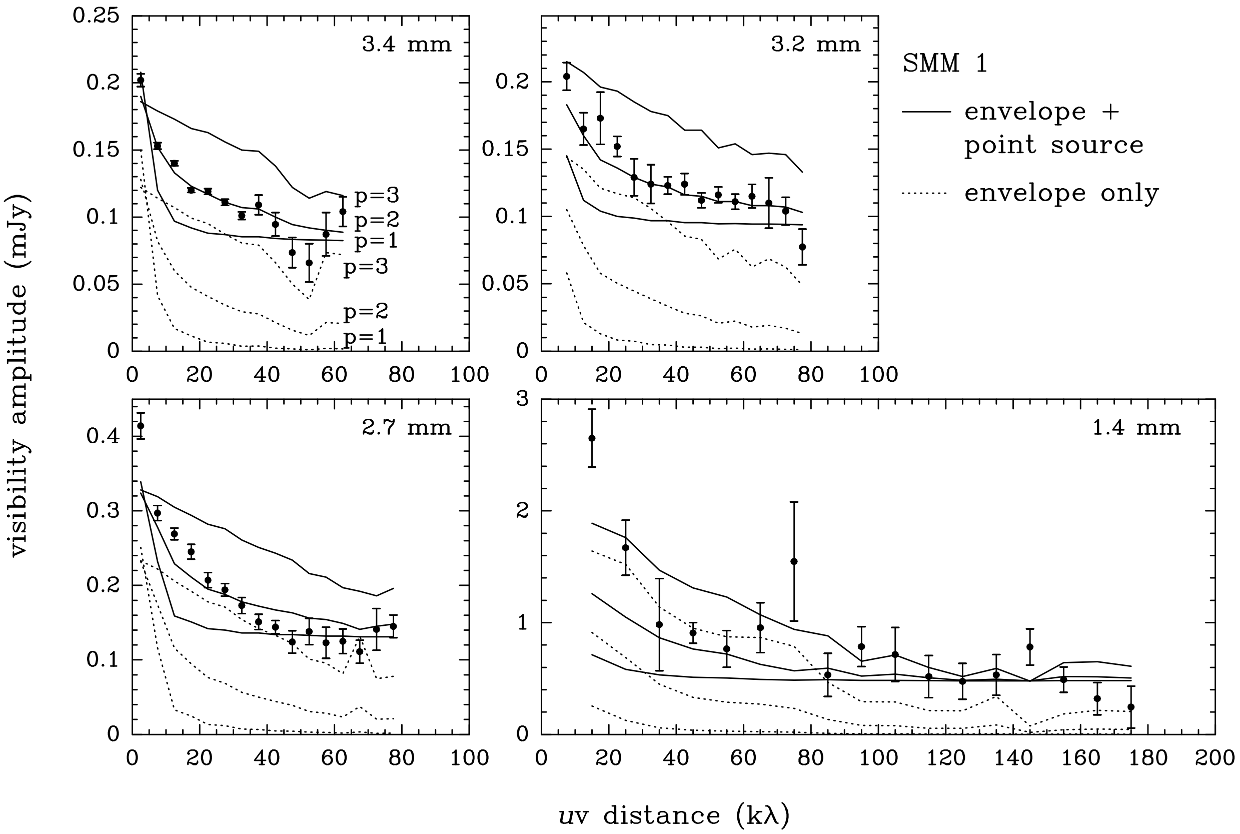

Fig. 6.3. *Comparison of model visibility amplitudes to observations of SMM 1. The observed vector-averaged amplitudes are indicated by the filled symbols and their 1σ error bars. Dotted lines are models without a central point source, and density power-law slopes of −1.0 (lower curve in each panel), −2.0 (middle curve), and −3.0 (upper curve). Solid lines are models with a point source flux of 0.13 Jy at 2.7 mm and a spectral slope of 2.0.*

on the adopted dust emissivity of Ossenkopf & Henning (1994), which is uncertain by approximately a factor of 2–3 (cf. also Agladze et al. 1994; Pollack et al. 1994). These masses exceed the limits placed on the stellar mass of 0.7–3.9 $M_\odot$ (SMM 1), 0.1–2.2 (SMM 3), and 0.1–2.3 $M_\odot$ (SMM 4; Table 6.1), confirming the young age of these sources and their classification as class 0 YSOs. The point-source fluxes constrain the masses within 100 AU to be 0.9, 0.4, and 0.5 $M_\odot$, respectively, for SMM 1, 3, and 4, assuming $T_\mathrm{d} \approx 100$ K. These masses are upper limits since the self-consistent temperature calculations suggest that the temperature exceeds 100 K by factors of a few at these small radii. In §6.4.2 the detection of highly excited lines of ^{12}CO, ^{13}CO, and H_2CO indicate the presence of $\sim$ 100 K material, corresponding to 0.5%–1% of the total envelope mass. This material could be responsible for a large fraction of the inferred point-source fluxes. A small fraction of the unresolved emission may originate in a circumstellar disk, but observations at much higher angular resolution are required to separate this from emission due to the inner envelope. Using single-baseline interferometry, Pudritz et al. (1996) infer a flux of 0.12 Jy at $\lambda = 1.4$ mm for a disk around the class 0 YSO VLA 1623 ($d = 160$ pc). Scaling to the distance of Serpens and

λ = 2.7 mm, this corresponds to only 5 mJy, suggesting that the fitted point-source emission toward these sources is dominated by compact envelope material.

6.4 Molecular line emission

6.4.1 Interferometer results

Compact emission is detected in most transitions observed toward the four sources. Figure 6.4 shows the naturally weighted, cleaned images of integrated intensity; Fig. 6.5 presents the spectra obtained within a $5'' \times 5''$ box around the image maximum, corresponding approximately to the synthesized beam. Table 6.4 lists the velocity-integrated brightness temperatures $\int T_b dV$ averaged over $5'' \times 5''$ and $20'' \times 20''$ regions around the source positions listed in Table 6.1. Estimates of the opacity averaged over the line profiles follow from the observed ratios of $C^{18}O/^{13}CO$, $H^{13}CO^+/HCO^+$, and $H^{13}CN/HCN$, and the relative intensities of the hyper-fine components of HCN and N_2H^+. Isotopic abundance ratios of $[^{13}CO]$:$[C^{18}O]$=8:1 and $[HCO^+]$:$[H^{13}CO^+]$=$[HCN]$:$[H^{13}CN]$=65:1 are assumed (Wilson & Rood 1994).

Extended ($\gtrsim 20''$) emission from optically thick material is resolved out by the interferometer in ^{13}CO, HCO^+, and HCN 1–0 toward all sources. This results in deep absorption features in the spectra of Fig. 6.5, and negative intensities in the images of Fig. 6.4. The level of resolved-out ^{13}CO 1–0 emission toward SMM 4 is so large that no positive signal is left in the integrated-intensity image. Using only the velocity interval of 4–8 km s^{-1}, where positive emission is detected, yields a core of $\sim 10''$ diameter around the source. Keeping in mind these high levels of resolved-out emission, the interferometer molecular line data can be interpreted, with caution, both qualitatively and quantitatively (cf. also §6.4.3).

As discussed in §6.2.1, the pointing centers of the observations of SMM 2, 3, and 4 are separated by only one primary-beam size, and care had to be taken to prevent emission spilling over in the deconvolved images. Figure 6.4 presents the cleaned images at the different transitions in single panels containing all three sources. The plotted images have been cleaned individually, since no reliable mosaic could be obtained with the pointing centers separated by a full primary beam. Maximum entropy deconvolution of the mosaicked images did yield consistent results, however.

None of the four sources show detectable emission in $C^{34}S$, while in C_3H_2 only a number of scattered clumps are detected toward SMM 1 and 4. The latter line probably traces dense condensations in the overall cloud, and is not further considered here. The upper limit of 3.9 K km s^{-1} on the emission of $C^{34}S$ toward SMM 1 is consistent with the weak detection of CS 2–1 toward this source of $\sim$ 6 K km s^{-1} by McMullin et al. (1994). Estimates of the molecular abundances on the scales traced by the interferometer are derived in §6.4.3 using detailed modeling of the molecular excitation, radiative transfer, and (u, v) sampling. Detailed analysis has shown that the derived abundances may be in error by as much as a factor of 5 if the intensities listed in Table 6.4 are used without going through this careful procedure (Chapter 7).

The following sections discuss the specific details of the aperture-synthesis results for the individual sources. In summary, the $C^{18}O$, ^{13}CO, and $H^{13}CO^+$ lines trace $5''$–$10''$

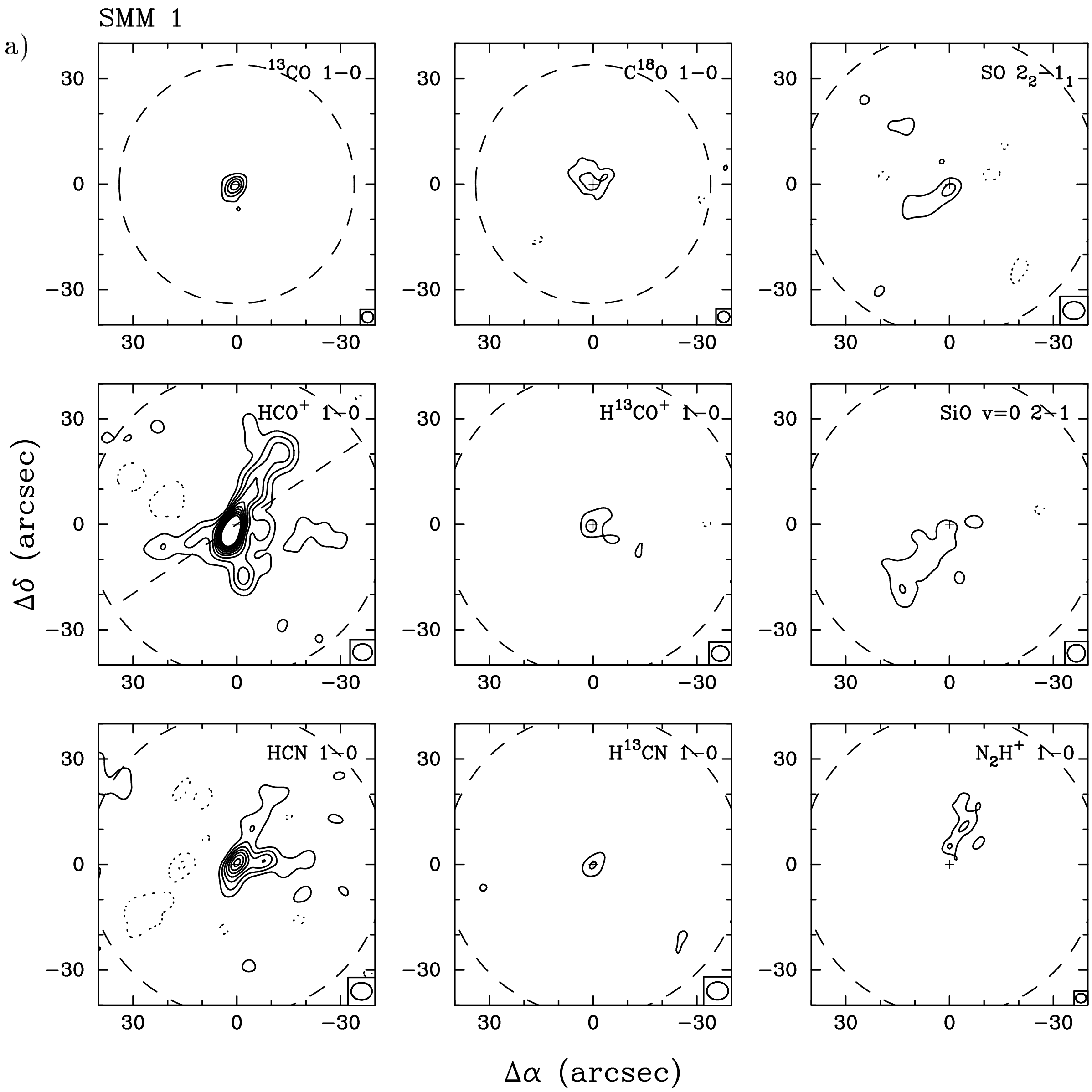

Fig. 6.4. (a) *Cleaned, naturally weighted images of molecular line emission observed with OVRO toward SMM 1. Contours are drawn at 3σ intervals. The synthesized beam size is indicated in each panel. The dashed circle shows the primary beam size. The straight line in the HCO$^+$ panel indicates the position angle of the jet.*

(2000–4000 AU) cores surrounding SMM 1, 3, and 4. The optically thick HCO$^+$ and HCN emission is associated with the walls of the outflow cavities, while SiO and SO probably reveal shocked material where the outflow impacts directly on the envelope. The physical regions traced by these lines are very similar to what has been observed toward other embedded YSOs (e.g., B5 IRS 1, Langer, Velusamy, & Xie 1996; B1, Hirano et al. 1997; and class I YSOs in Taurus, Chapter2, Hogerheijde et al. 1997a). SMM 2 does not show any compact emission, consistent with the interpretation that this core does not contain a protostar.

b) SMM 2, SMM 3, and SMM 3

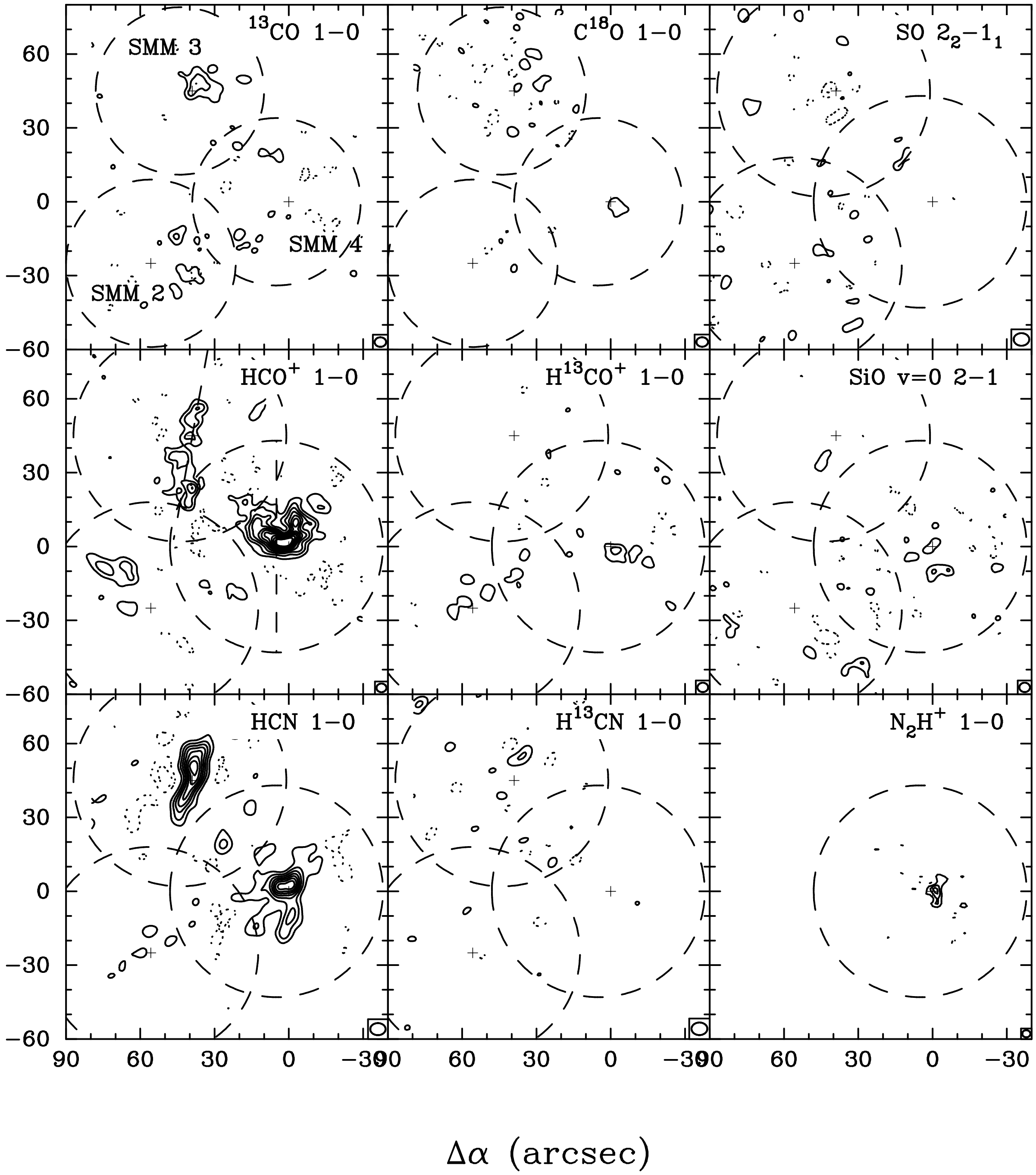

Fig. 6.4 (b) *Same, for SMM 2, 3, and 4. The images have been cleaned separately, and mosaicked afterwards.*

6.4.1.1 SMM 1

A compact, $\sim 10''$ (4000 AU) diameter core around SMM 1 is traced by the OVRO observations of $C^{18}O$, $H^{13}CO^+$, and $H^{13}CN$ 1–0. Assuming local thermodynamic equilibrium (LTE), a fiducial estimate of the kinetic temperature of 30 K, and a $C^{18}O$ abundance

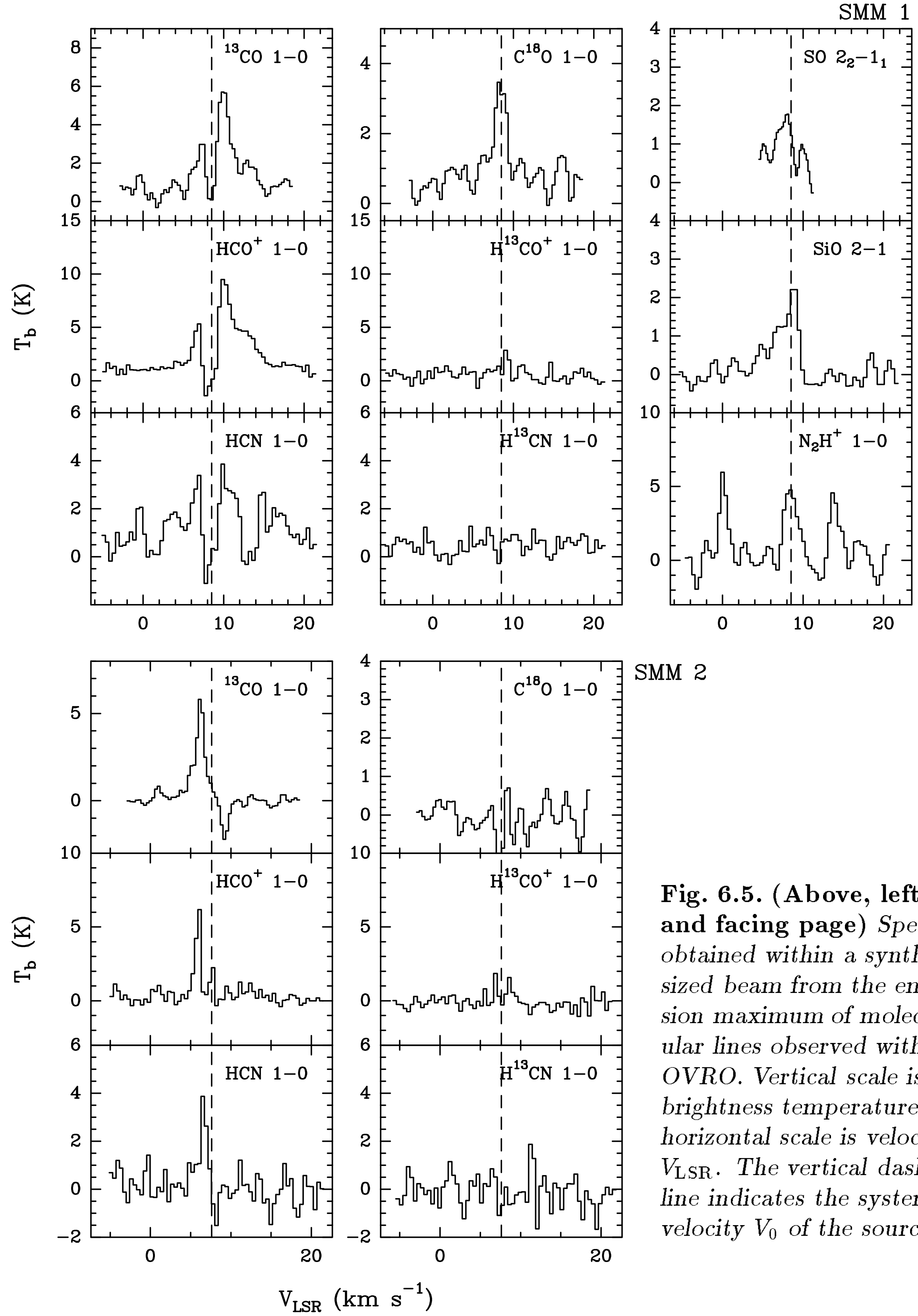

Fig. 6.5. (Above, left, and facing page) *Spectra obtained within a synthesized beam from the emission maximum of molecular lines observed with OVRO. Vertical scale is brightness temperature T_b, horizontal scale is velocity V_{LSR}. The vertical dashed line indicates the systemic velocity V_0 of the source.*

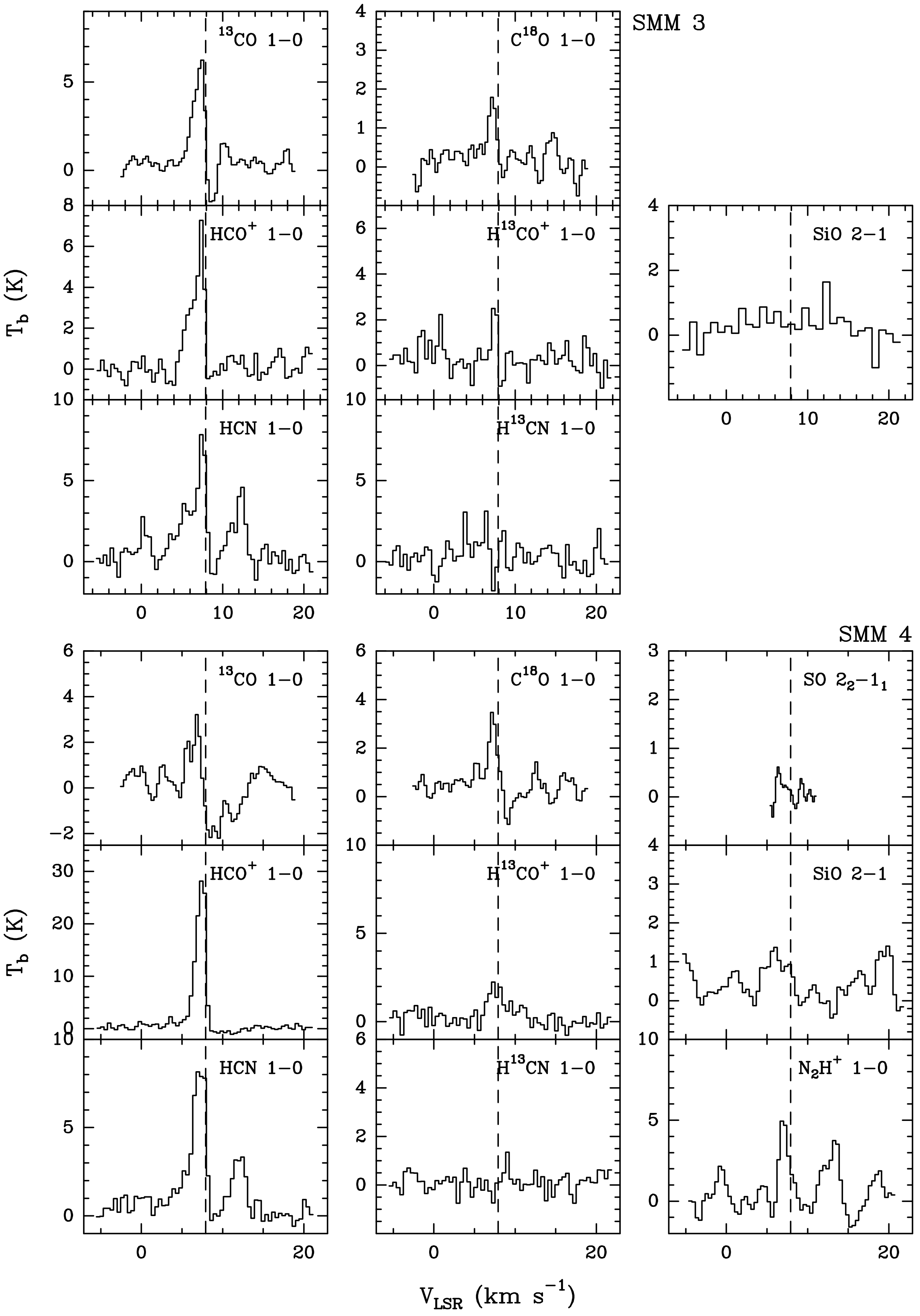
SMM 3
13CO 1–0
C18O 1–0
HCO+ 1–0
H13CO+ 1–0
SiO 2–1
HCN 1–0
H13CN 1–0
SMM 4
13CO 1–0
C18O 1–0
SO 22–11
HCO+ 1–0
H13CO+ 1–0
SiO 2–1
HCN 1–0
H13CN 1–0
N2H+ 1–0
Tb (K)
VLSR (km s−1)

with respect to H_2 of 2×10^{-7}, a mass of 0.25 $M_\odot$ is inferred over a $20'' \times 20''$ region. Although this appears much less than the mass of 8.7 $M_\odot$ inferred from the dust emission in §6.3.2, modeling in §6.4.3 indicates that for the derived envelope parameters only such a low fraction of the mass is recovered through $C^{18}O$ emission in the OVRO beam.

The emission from optically thick HCO^+, HCN, and ^{13}CO lines appears to be directly associated with the outflow. Because of the large level of resolved-out emission in these lines, only red- and blueshifted material is traced by the interferometer, whereas the bulk of the emission from the envelope is not seen. This is especially apparent in ^{13}CO, where only unresolved emission is recovered, but with a total velocity width of almost 10 km s^{-1}. The emission of HCO^+ and HCN apparently traces the walls of the outflow cavity. The position angle of the outflow is constrained by radio measurements to roughly $-50°$ (Rodríguez et al. 1989), bisecting the two arms seen in HCN, and the roughly cross-shaped HCO^+ emission. Only the peak of the emission, centered on the protostar, has a velocity extent of $\sim$ 20 km s^{-1} in the HCO^+ and HCN spectra. The extended arms lie within $\sim$ 5 km s^{-1} of the systemic velocity. H_2 emission at 2.2 μm coincides with the northern HCO^+ and HCN arm, probably tracing shocked material along the wall of the outflow (cf. Rodríguez et al. 1989). N_2H^+ 1–0 emission also traces this northern outflow wall.

Emission from SiO 2–1 and SO 2_2–1_1 coincides with the southeast outflow lobe. The prominent blue line wing in the spectrum at the emission peak at the southeast tip of the lobe clearly shows the association of SiO with material in the outflow. Using the $C^{18}O$ upper limit at the peak of the SiO and SO emission, and assuming LTE excitation at $\sim$ 100 K, yields lower limits to the abundance of a few times 10^{-8} for SiO and $\sim 10^{-7}$ for SO. Such enhanced abundances of SiO and SO are attributed to shocked material (cf. Bachiller 1996; van Dishoeck & Blake 1998). More accurate constraints on the SiO and SO abundances require that the missing zero-spacing flux of SiO, SO, and $C^{18}O$ be taken into account. Such detailed modeling is also required to investigate the relation between the material traced in SiO and SO compared to HCO^+ and HCN.

In ^{12}CO 2–1 maps presented by White et al. (1995) the outflow shows a complicated structure with the northwestern outflow lobe being mostly blueshifted, while the southeastern lobe shows both red- and blueshifted emission. The small scale structure associated with the outflow also is markedly asymmetric. In H_2 at 2.2 μm, and in HCO^+ and N_2H^+ in the OVRO beam the northern cavity wall is most prominent, while HCN only traces the northern and western walls. SiO and SO emission trace the southeastern outflow lobe. This asymmetry might be explained by a large-scale density gradient in the ambient medium, with denser material located to the east, coincident with the location of the bulk of the Serpens cloud. In such a medium, the time scale to clear an outflow cavity to the southeast may be longer than that to the northwest. SiO and SO emission trace shock interaction of the latter outflow lobe with ambient material, while the larger column of material is optically thick to any associated HCO^+ or HCN emission. For $n_{H_2} \approx 10^6$ cm^{-3} and $T_{kin} \approx 30$ K, a column of a few times 10^{14} cm^{-2} in HCO^+ or HCN is sufficient for the required level of obscuration. With the envelope parameters derived in §6.3.2, this corresponds to a density contrast of a factor of a few between both sides of the envelope. To the northeast, HCO^+ and HCN emission arises

Table 6.4. OVRO integrated intensities and line opacities

		5″ × 5″ area		20″ × 20″ area	
Source	Line	$\int T_{\rm b} dV$ (K km s^{-1})	$\bar{\tau}$	$\int T_{\rm b} dV$ (K km s^{-1})	$\bar{\tau}$
SMM 1	^{13}CO 1–0	27.1 ± 0.3	2.1	2.49 ± 0.08	6.5
	C^{18}O 1–0	7.4 ± 0.1	0.3	1.38 ± 0.03	0.8
	C^{34}S 2–1	< 3.9	...	< 1.0	...
	C_3H_2 4_{32}–4_{23}	2.0 ± 0.1	...	0.34 ± 0.02	...
	HCO$^+$ 1–0	48.4 ± 0.1	19.5	14.0 ± 0.03	7.7
	H^{13}CO$^+$ 1–0	12.5 ± 0.2	0.3	1.56 ± 0.06	0.1
	HCN 1–0	22.0 ± 0.1	15.5	4.96 ± 0.03	5.3
	H^{13}CN 1–0	4.7 ± 0.1	0.2	0.39 ± 0.03	0.1
	N_2H^+ 1–0	1.4 ± 0.1	...	3.79 ± 0.22	2 ± 1
	SiO 2–1	3.9 ± 0.1	...	1.62 ± 0.03	...
	SO 2_2–1_1	2.0 ± 0.1	...	0.43 ± 0.01	...
SMM 2	^{13}CO 1–0	< 0.5	...	0.25 ± 0.05	< 5.5
	C^{18}O 1–0	< 0.3	...	< 0.1	< 0.7
	C_3H_2 4_{32}–4_{23}	< 0.4	...	< 0.10	...
	HCO$^+$ 1–0	< 0.5	...	0.64 ± 0.04	...
	H^{13}CO$^+$ 1–0	1.2 ± 0.1	...	1.23 ± 0.03	...
	HCN 1–0	1.2 ± 0.2	...	1.53 ± 0.04	5 ± 4
	H^{13}CN 1–0	< 0.8	...	< 0.2	< 0.1
	SiO 2–1	< 1.3	...	< 0.3	...
	SO 2_2–1_1	< 0.5	...	< 0.1	...
SMM 3	^{13}CO 1–0	11.8 ± 0.2	< 5.5	3.37 ± 0.05	< 0.2
	C^{18}O 1–0	< 0.45	< 0.7	< 0.15	< 0.1
	C_3H_2 4_{32}–4_{23}	< 0.33	...	< 0.12	...
	HCO$^+$ 1–0	9.3 ± 0.2	< 2.4	4.07 ± 0.05	< 1.1
	H^{13}CO$^+$ 1–0	< 0.36	< 0.04	< 0.1	< 0.1
	HCN 1–0	33.2 ± 0.2	< 0.5	12.8 ± 0.06	2.8
	H^{13}CN 1–0	< 0.9	< 0.1	0.7 ± 0.1	3.5
	SiO 2–1	< 1.8	...	< 0.51	...
	SO 2_2–1_1	< 0.4	...	< 0.1	...
SMM 4	^{13}CO 1–0	< 0.75	...	< 0.21	...
	C^{18}O 1–0	4.4 ± 0.1	...	0.82 ± 0.02	...
	C^{34}S 2–1	< 5.0	...	< 1.5	...
	C_3H_2 4_{32}–4_{23}	0.5 ± 0.1	...	< 0.06	...
	HCO$^+$ 1–0	40.8 ± 0.2	9.3	18.0 ± 0.06	4.2
	H^{13}CO$^+$ 1–0	5.4 ± 0.1	0.1	1.13 ± 0.04	< 0.1
	HCN 1–0	31.4 ± 0.2	< 0.5	13.3 ± 0.04	< 0.2
	H^{13}CN 1–0	< 0.6	< 0.1	< 0.15	< 0.1
	N_2H^+ 1–0	7.8 ± 1.2	< 2.0	< 1.0	...
	SiO 2–1	< 1.2	...	0.28 ± 0.11	...
	SO 2_2–1_1	< 0.3	...	< 0.06	...

in the walls surrounding a relatively empty outflow cavity, and H_2 2 μm emission is observable where the outflow breaks out of the cloud.

6.4.1.2 SMM 2

SMM 2 only shows emission in ^{13}CO, HCO$^+$, H^{13}CO$^+$, and HCN from clumps scattered throughout the field of view. The spectra toward the emission peaks reveal narrow lines of 1 km s^{-1} width, except for ^{13}CO. This lack of central condensation is consistent with the upper limit on the continuum emission from §6.3.1, and supports the interpretation that the SMM 2 core does not contain a protostar. Instead, the interferometer appears to trace irregular structure in the extended cloud, with most of the emission distributed on large, resolved-out scales.

6.4.1.3 SMM 3

The ^{13}CO emission toward this source traces a $10''$ (4000 AU) diameter core around the continuum position, with a mass of 0.08 $M_\odot$, while only weak emission is detected in C^{18}O. Model calculations in §6.4.2 confirm that only a small fraction of the 3.0 $M_\odot$ envelope is recovered in ^{13}CO emission in the OVRO beam. The HCO$^+$ and HCN images show elongated emission extending over $\sim 30''$ at a position angle of $-20°$. Herbst et al. (1997a) have detected a string of H_2 emission knots along a line with the same orientation, which they attribute to a jet. In this interpretation, HCO$^+$ and HCN trace a highly collimated outflow. A marginally detected SiO core coincides with the south end of the outflow. The high degree of collimation of the outflow may indicate that SMM 3 is a particularly young YSO. Together with the projected location of SMM 3 on the edge of the outflow of SMM 4 (see below, and Fig. 6.4), this may suggest induced star formation.

Although the visual extinction toward SMM 3 is still very large, it does have the lowest inferred envelope mass of the three YSOs. It is therefore probably less deeply embedded than SMM 1 or 4, based on the weak detection of C^{18}O, the upper limits on H^{13}CO$^+$, and the relatively shallow absorption features in the spectra. Weak H^{13}CN emission coincides with the northern outflow lobe, indicating that HCN may be strongly enhanced by the outflow.

6.4.1.4 SMM 4

The C^{18}O, H^{13}CO$^+$, and N$_2$H$^+$ emission traces a $5''$–$10''$ (2000–4000 AU) core around this source with a mass of 0.15 $M_\odot$. As for SMM 1 and 3, modeling in §6.4.2 indicates that the amount of material traced by C^{18}O in the OVRO beam is consistent with the parameters of the 5.3 $M_\odot$ envelope derived in §6.3.2. As explained above, the integrated ^{13}CO intensity image does not show any emission, because of the large optical depth of resolved-out extended emission, so that the ^{13}CO spectrum reveals a deep absorption feature close to the systemic velocity.

In HCO$^+$ and HCN the emission is again associated with the outflow. The ^{12}CO 2–1 single-dish observations of White et al. (1995) indicate a north–south orientation. Eiroa et al. (1997) present 2.2 μm observations showing a possible H_2 jet with a position angle of $\sim 10°$ emanating from SMM 4. HCO^+ emission outlines the northern outflow cavity, while HCN also traces the southern outflow lobe. In addition, strong emission originates from a $10''$ core, elongated perpendicular to the outflow direction. The bulk of the HCO^+ and HCN emission occurs within 2–4 km s^{-1} from line center, as seen in the spectra. This indicates that the HCO^+ and HCN lines trace envelope material which is heated, compressed, or chemically altered by the outflow, but not entrained within the outflow itself. In HCO^+ there is a 4 km s^{-1} west-to-east velocity gradient, possibly indicating rotation in the envelope and cavity walls. The hyperfine components in the HCN line confuse any velocity gradient in that line. The fact that HCO^+ emission is associated with the northern outflow lobe only may be connected to a higher outflow or interaction activity on that side. The ^{12}CO 2–1 outflow maps of White et al. (1995) also show more intense outflow emission toward the north of SMM 4. A number of marginally detected clumps of SiO are seen close to the center of SMM 4, but no SO is found.

6.4.2 Single-dish results

In this section we will discuss the results of the single-dish observations. Figure 6.6 shows the spectra obtained toward the source positions. The velocity-integrated maps are presented in Fig. 6.7. Table 6.5 lists the integrated line intensities in all observed transitions, together with estimates of the opacity averaged over the line profile. These are derived from measurements of the same transition in different isotopes, assuming isotope ratios of $[^{13}C] : [^{12}C] = 1 : 65$ and $[^{18}O] : [^{17}O] : [^{16}O] = 6 : 1 : 2695$ (Wilson & Rood 1994). Opacities at line center are much larger, as evidenced by deep self-absorption features in many lines.

The observed line profiles of ^{12}CO, HCO^+, and HCN are characterized by $\sim$ 20–30 km s^{-1} wide line wings and deep, narrow ($\sim$ 1–2 km s^{-1}) self-absorption features, in addition to 2–4 km s^{-1} FWHM line cores. Toward SMM 3 and 4 the blue asymmetry characteristic of infall is present in the ^{12}CO and HCO^+ lines (cf. Gregersen et al. 1997). The same lines toward SMM 1 show symmetric profiles, however. In optically thin tracers like $H^{13}CO^+$, $C^{18}O$, $C^{17}O$, and $H^{13}CN$ only a simple Gaussian line of $\sim$ 2 km s^{-1} FWHM is seen. From the $C^{17}O$ and $C^{18}O$ lines systemic velocities of the sources are derived to be +8.5 km s^{-1} (SMM 1), +7.6 km s^{-1} (SMM 2), +7.9 km s^{-1} (SMM 3), and +7.9 km s^{-1} (SMM 4). The ^{13}CO lines show moderate self-absorption as well as $\sim$ 10 km s^{-1} wide line wings. Many of the other observed transitions show simple Gaussian line profiles, although some lines (e.g., H_2CO 3_{03}–2_{02} and 3_{22}–2_{21}) are unresolved at the observed velocity resolution. Hurt et al. (1996b) present observations of these lines at higher spectral resolution, which reveal moderate self-absorption features. The integrated line intensities are unaffected, as long as the overall line width is still comparable to the instrumental resolution.

The ^{12}CO 4–3 and 6–5 line profiles plotted in Fig. 6.6 reveal an interesting hint about the temperature and velocity structure of the outflowing gas. While the line wings in ^{12}CO 4–3 decrease smoothly to more red- and blueshifted velocities, the ^{12}CO 6–5 wings show secondary maxima at $\sim$ 7–9 km s^{-1} from the systemic velocity. This indicates that the excitation temperature of the gas increases with velocity in the outflow, to $\gtrsim$200 K at the velocity of the secondary maxima in ^{12}CO 6–5. In addition, a larger

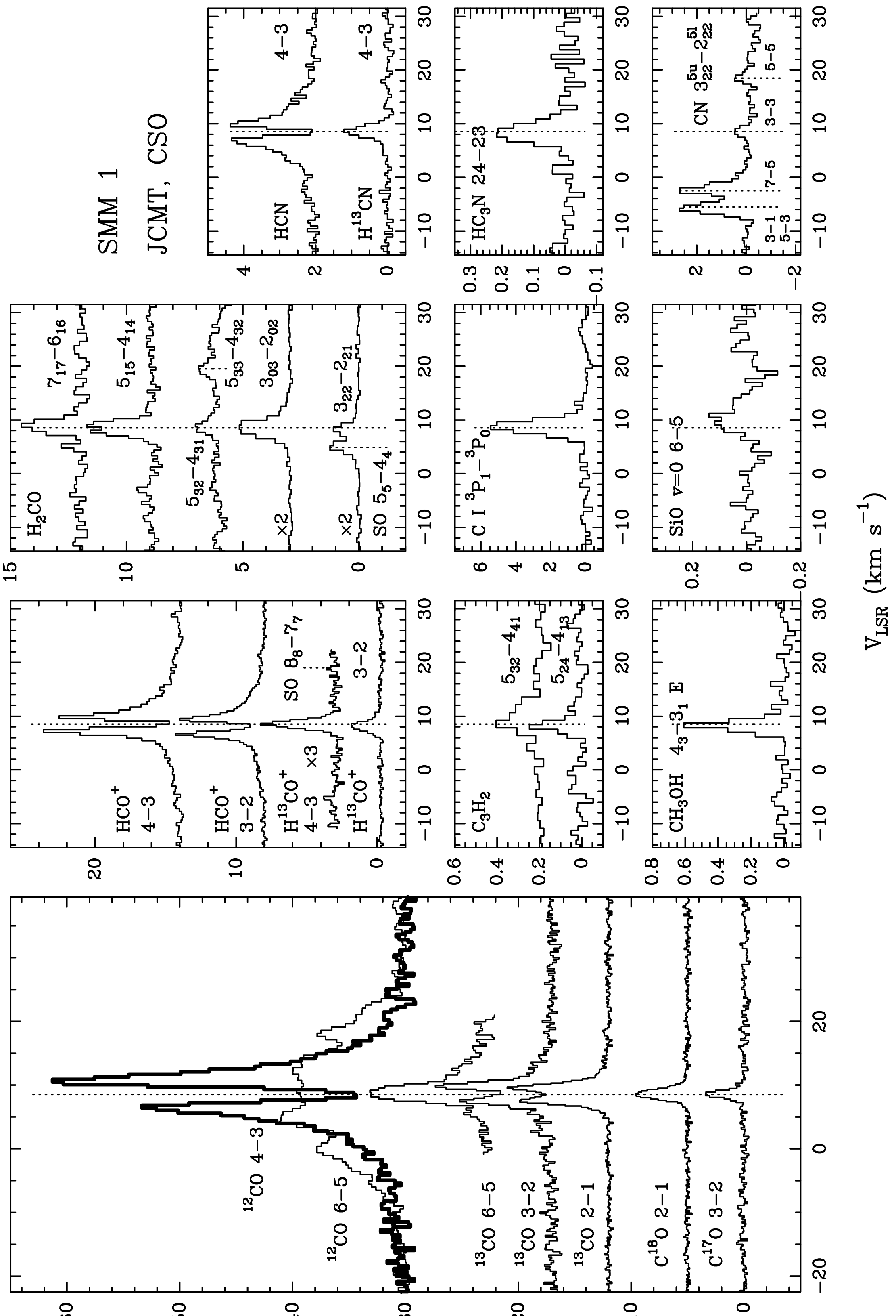

Fig. 6.6. **(a)** *Single-dish spectra of SMM 1. Vertical scale in $T_{\rm bm}$ in K. The dotted line idnicates the systemic velocity.*

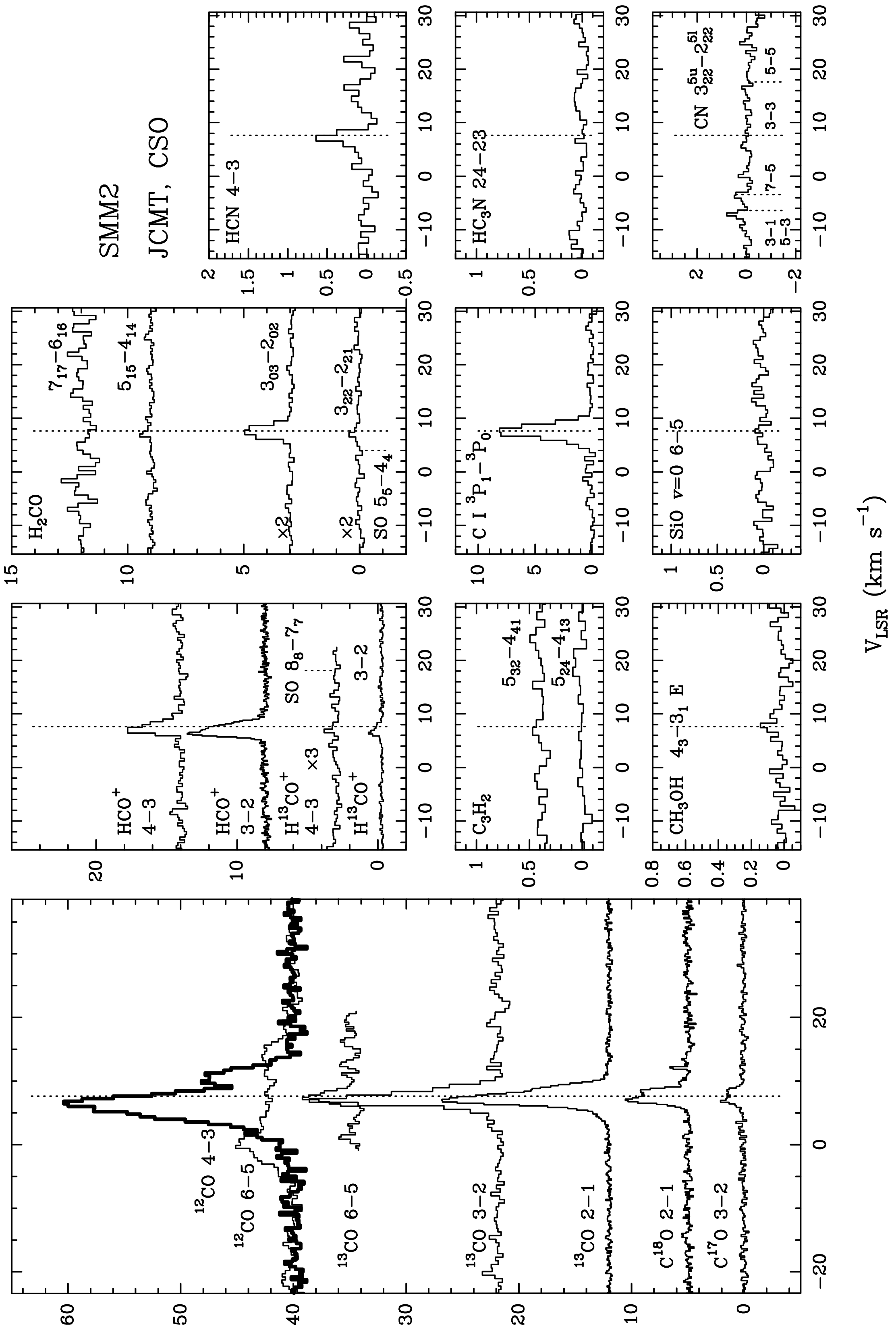

Fig. 6.6. (b) *Single-dish spectra of SMM 2.*

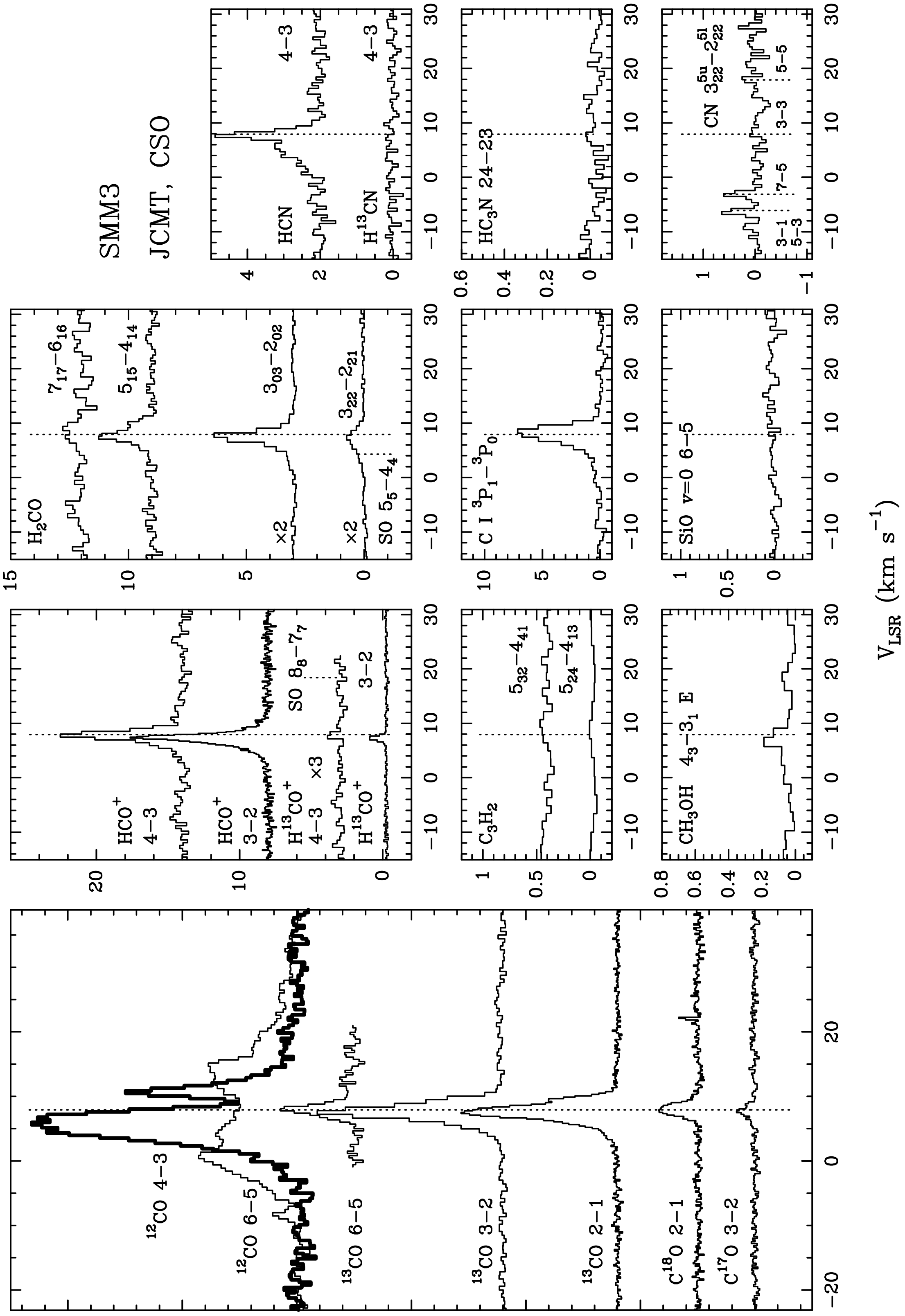

Fig. 6.6. (c) *Single-dish spectra of SMM 3.*

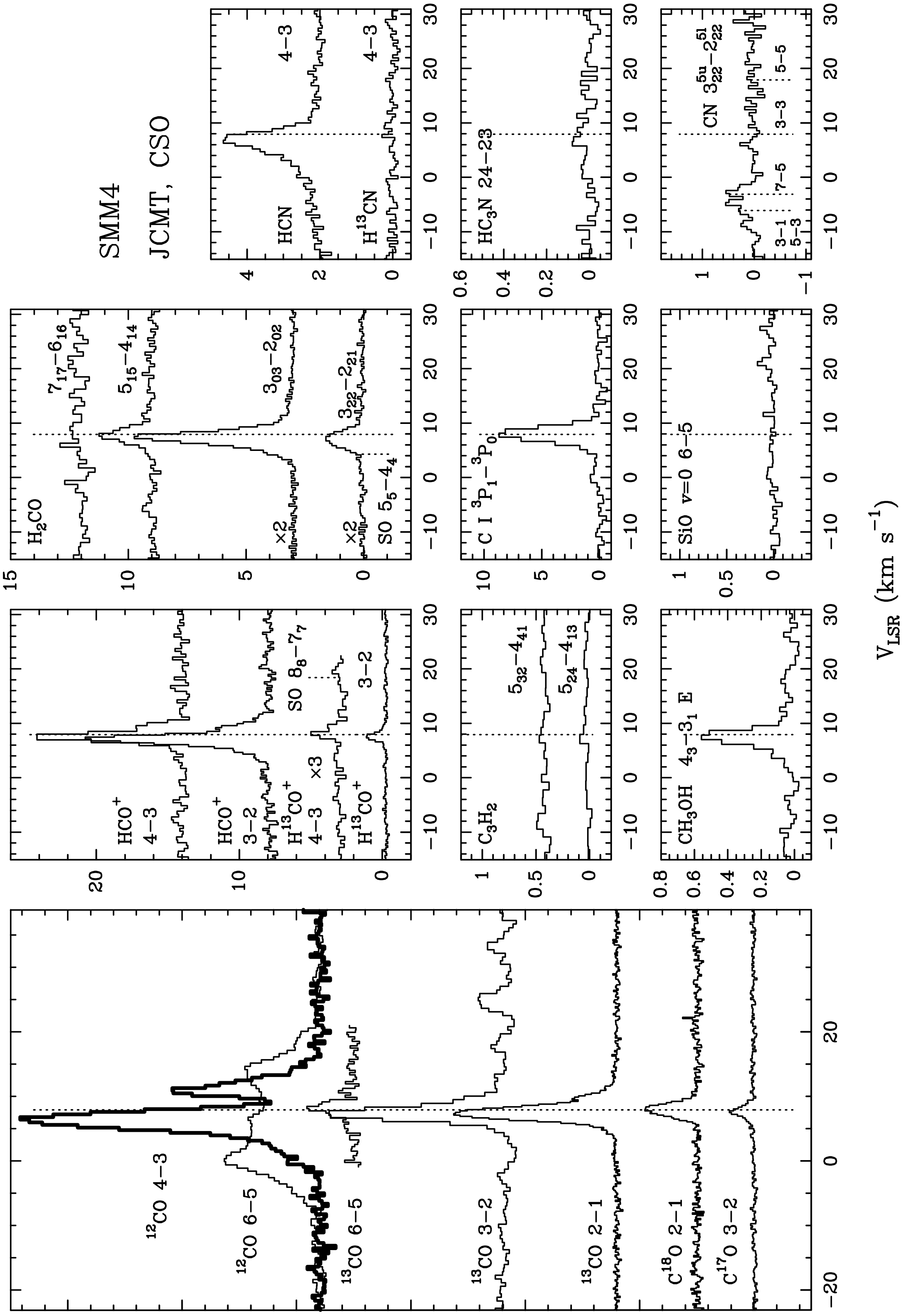

Fig. 6.6. **(d)** *Single-dish spectra of SMM 4.*

a)

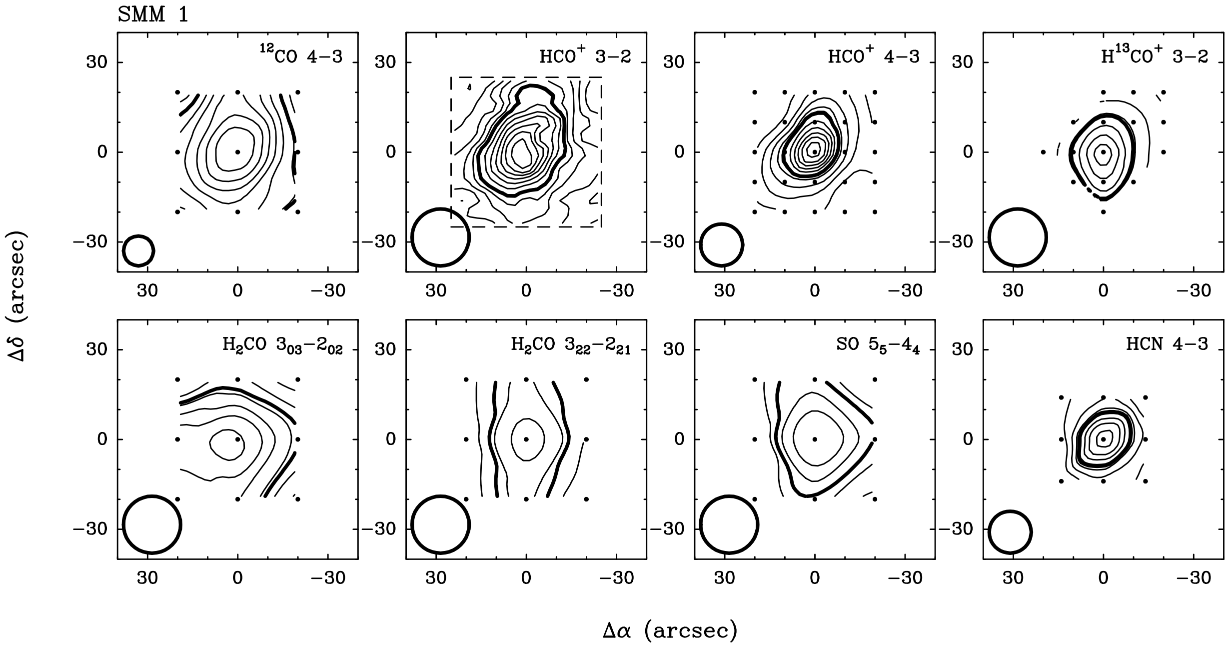

Fig. 6.7. (a) *Maps of integrated intensity observed with the JCMT toward SMM 1. Sampling is indicated by the small dots, except for HCO$^+$ 3–2, which is fully sampled. The dashed lines shows the extent of the mapped region. The beam sizes are indicated in each panel. Contours are drawn at approximately 3σ intervals. The thick contour indicates the 50% of maximum intensity level.*

fraction of the 6–5 line cores is self-absorbed as compared to the 4–3 lines. The ^{12}CO 6–5 line profiles toward the low-mass YSO TMC 1A in Taurus show a similar secondary maximum in the blue line wing (Chapter 3, Hogerheijde et al. 1998a).

The maps of integrated intensity show well-defined cores around the positions of SMM 1, 3, and 4. Again, SMM 2 appears associated with a condensation in the overall cloud rather than a YSO. Still, SMM 2 does show ^{12}CO 6–5 emission with broad line wings, which requires kinetic temperatures of 80 K or more to be excited, as well as the secondary maxima noted above. White et al. (1995) conclude from ^{12}CO 2–1 mapping that outflow emission permeates the whole Serpens cloud core region. Probably, the ^{12}CO 6–5 lines are tracing this same material at the position of SMM 2 with the same distribution of excitation temperature with velocity. The ^{12}CO 4–3, and HCO$^+$ 3–2 and 4–3 maps toward SMM 1, 3, and 4 are resolved with diameters of 20″–30″ (8000–12000 AU), while H^{13}CO$^+$ 3–2 (SMM 1) and HCN 4–3 (SMM 1 and 4) appear unresolved at the respective beam sizes of 19″ (7600 AU) and 14″ (5600 AU). The maximum of the emission in ^{12}CO 4–3 toward SMM 4 is offset by $\sim$ 15″ to the north. The five-point map observed in ^{12}CO 6–5 shows a similar offset. These lines probably trace $T_{\rm kin} \approx 100$ K gas associated with the outflow. Absorption of a significant fraction of the line profiles by cold and dense envelope material within $\sim$ 15″ from the YSO could explain the apparent offsets of the peak in the integrated intensity maps.

The detection of many highly excited lines of ^{12}CO, HCO$^+$, HCN, and H$_2$CO indicates kinetic temperatures as high as 50–100 K. The line ratio of H$_2$CO 3$_{03}$–2$_{02}$ over 3$_{22}$–2$_{21}$ is a very sensitive diagnostic of kinetic temperature (Mangum & Wootten 1993;

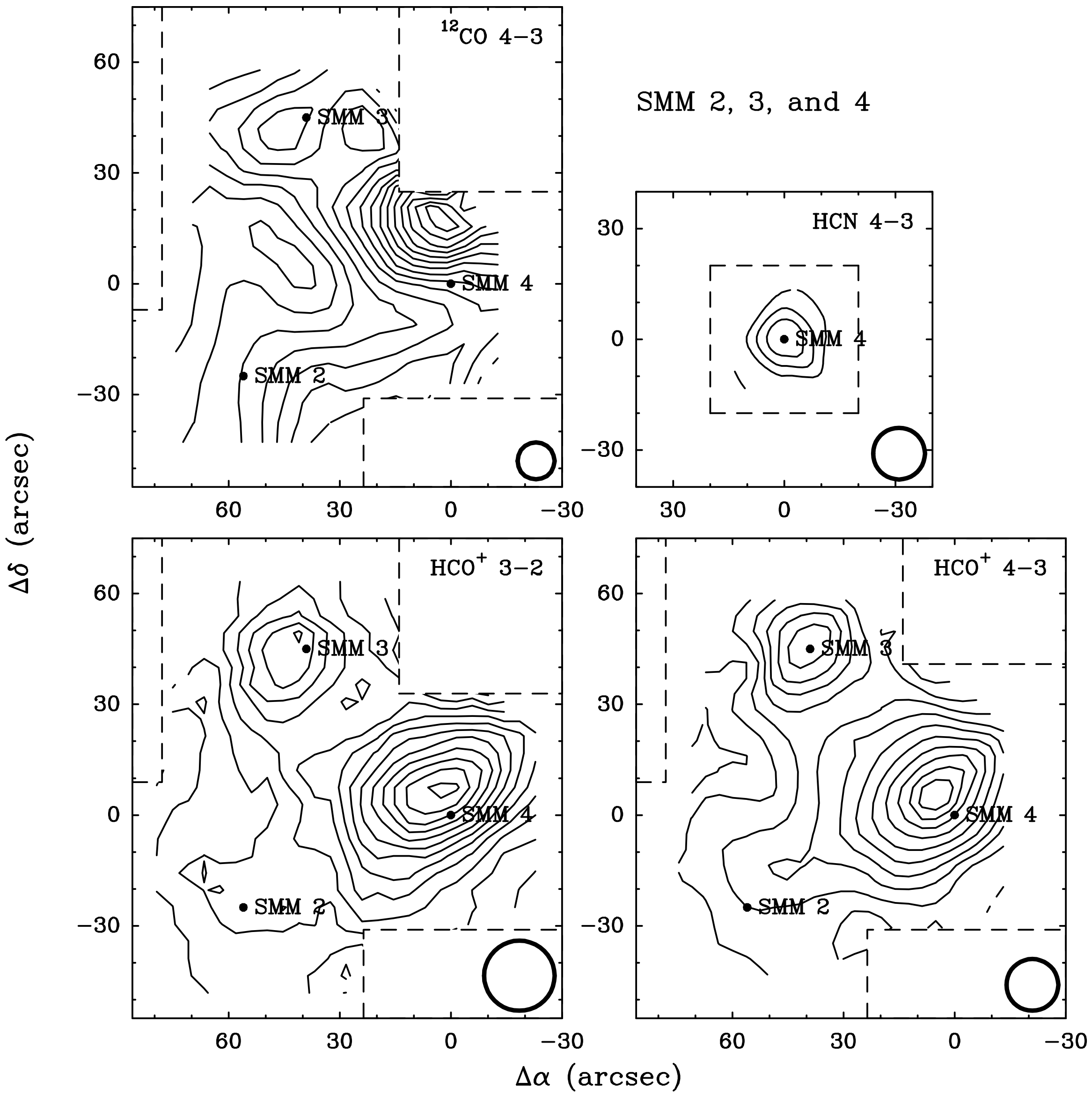

Fig. 6.7. (b) *Single-dish maps of SMM 2, 3, and 4. The sampling, identical to that for SMM 1, is not indicated for clarity.*

Jansen, van Dishoeck, & Black 1994; Hurt et al. 1996b). Our data imply a gas density in excess of 10^6 cm^{-3}, as indicated by the detection H_2CO 5_{15}–4_{14} and 7_{17}–6_{16}, and a kinetic temperature of 50–200 K for the material traced by the H_2CO lines, consistent with the findings of Hurt et al. (1996b). The observed integrated intensity of ^{13}CO 6–5 and of the ^{12}CO 4–3 and 6–5 line wings corresponds to a column of 100 K gas in a $10''$ beam of $\sim 9 \times 10^{21}$ cm^{-2} for SMM 1, and $\sim 7 \times 10^{20}$ for SMM 3 and 4. This is only 0.5%–1% of the total envelope mass, contributing no more than 10% to the total continuum flux. If extended over less than 1000 AU ($< 3''$), it could explain the point sources required to fit the interferometer continuum observations (§6.3.2), which carry comparable fractions (20%–30%) of the total flux.

Table 6.5. Single-dish integrated line intensities and opacities

Line	SMM 1	SMM 2	SMM 3	SMM 4
	Integrated intensities $\int T_{\rm mb} dV$ (K km s^{-1})			
^{12}CO 4–3	232.2 ± 2.2	120.6 ± 1.7	171.3 ± 1.8	148.5 ± 1.6
^{12}CO 6–5	221.9 ± 2.7	60.1 ± 1.8	165.7 ± 2.0	134.5 ± 1.4
^{13}CO 2–1	27.0 ± 0.2	40.8 ± 0.3	43.1 ± 0.3	42.8 ± 0.3
^{13}CO 3–2	35.8 ± 0.6	39.9 ± 0.8	50.1 ± 0.6	45.7 ± 0.7
^{13}CO 6–5	41.4 ± 1.0	5.6 ± 0.7	12.8 ± 0.6	9.2 ± 0.5
C^{18}O 2–1	9.5 ± 0.2	13.0 ± 0.3	7.7 ± 0.3	11.0 ± 0.3
C^{17}O 3–2	5.7 ± 0.3	4.9 ± 0.2	3.0 ± 0.2	4.2 ± 0.2
HCO$^+$ 3–2	33.3 ± 0.4	13.1 ± 0.2	21.8 ± 0.3	36.0 ± 0.5
HCO$^+$ 4–3	48.1 ± 0.7	8.8 ± 0.5	20.4 ± 0.8	25.0 ± 0.6
H^{13}CO$^+$ 3–2	5.8 ± 0.2	1.7 ± 0.1	1.6 ± 0.8	2.9 ± 0.1
H^{13}CO$^+$ 4–3	3.1 ± 0.1	< 0.4	0.2 ± 0.1	1.2 ± 0.1
HCN 4–3	17.5 ± 0.4	1.4 ± 0.3	10.1 ± 0.3	14.0 ± 0.4
H^{13}CN 4–3	3.0 ± 0.2	...	< 0.8	< 0.5
H$_2$CO 3_{03}–2_{02}	4.6 ± 0.1	2.7 ± 0.1	4.9 ± 0.1	11.0 ± 0.1
H$_2$CO 3_{22}–$2_{21}$$^{\rm b}$	1.8 ± 0.1	0.4 ± 0.1	1.7 ± 0.1	2.93 ± 0.1
H$_2$CO 5_{15}–4_{14}	8.0 ± 0.3	0.7 ± 0.2	7.2 ± 0.3	6.4 ± 0.3
H$_2$CO 5_{32}–4_{31}	3.3 ± 0.3	...	...	...
H$_2$CO 5_{33}–4_{32}	2.8 ± 0.3	...	...	...
H$_2$CO 7_{17}–6_{16}	6.7 ± 0.6	< 1.5	< 1.3	< 1.6
C I ^{3}P$_1$–^{3}P$_0$	18.0 ± 0.7	26.7 ± 1.0	30.3 ± 1.0	29.8 ± 0.9
C$_3$H$_2$ 5_{24}–4_{13}	0.7 ± 0.1	< 0.3	< 0.2	< 0.2
C$_3$H$_2$ 5_{32}–4_{41}	1.0 ± 0.1	< 0.3	< 0.2	< 0.3
CH$_3$OH 4_2–3_1 E	1.4 ± 0.1	< 0.3	0.6 ± 0.1	2.1 ± 0.1
HC$_3$N 24–23	0.9 ± 0.1	< 0.5	< 0.2	< 0.2
CN $3\frac{5}{2}\frac{3}{2}$–$2\frac{3}{2}\frac{1}{2}$, $\frac{5}{2}$–$\frac{3}{2}$$^{\rm c}$	6.6 ± 0.3	1.4 ± 0.2	0.7 ± 0.2	1.4 ± 0.2
CN $3\frac{5}{2}\frac{3}{2}$–$2\frac{3}{2}\frac{3}{2}$	0.8 ± 0.2	< 0.6	< 0.6	< 0.5
CN $3\frac{5}{2}\frac{5}{2}$–$2\frac{3}{2}\frac{5}{2}$	< 0.8	< 0.6	< 0.6	< 0.5
CN $3\frac{5}{2}\frac{7}{2}$–$2\frac{3}{2}\frac{5}{2}$$^{\rm c}$	6.0 ± 0.2	< 0.6	0.6 ± 0.2	0.8 ± 0.2
SO 5_5–$4_4$$^{\rm b}$	1.4 ± 0.1	< 0.3	< 0.1	< 0.2
SO 8_8–7_7	0.3 ± 0.1	< 0.3	0.3 ± 0.1	< 0.3
SiO 6–5	< 0.4	< 0.3	< 0.2	< 0.3

6.4.3 A model for the molecular line emission

In the previous section we constructed a model for the envelope from the dust continuum emission, with a density distribution characterized by a power law with index -2.0 and a dust temperature distribution following a power law with a slope of -0.4. At radii smaller than $\sim$ 450 AU this slope steepens to -0.9. More than 95% of the material in these envelopes has a dust temperature of less than 50 K. In this section we will investigate whether the observed molecular line emission, and the highly excited lines

Table 6.5. (continued)

Line	SMM 1	SMM 2	SMM 3	SMM 4
		Opacities $\bar{\tau}^{\rm d}$		
^{12}CO 6–5	13.5	6.4	5.2	4.6
^{13}CO 2–1	3.4	5.5	0.9	2.0
^{13}CO 3–2	7.3	5.5	2.4	4.0
^{13}CO 6–5	0.2	0.1	0.1	0.1
C^{18}O 2–1	0.4	0.3	0.1	0.3
C^{17}O 3–2	0.2	0.1	0.1	0.1
HCO$^+$ 3–2	12.4	9.1	5 ± 3	5.5
HCO$^+$ 4–3	4.3	< 3.1	< 0.2	3.0
H^{13}CO$^+$ 3–2	0.2	0.1	0.1	0.1
H^{13}CO$^+$ 4–3	0.1	< 0.1	< 0.1	0.1
HCN 4–3	12.3	...	< 0.2	< 2.1
H^{13}CN 4–3	0.2	...	< 0.1	< 0.1

[a] Upper limits are 3σ.

[b] H_2CO 3_{22}–2_{21} and SO 5_5–4_4 are partially blended. Assuming equal contributions for SMM 1, and no contribution from SO for SMM 2, 3, and 4 (cf. spectra in Fig. 6.6).

[c] CN $3\frac{5}{2}\frac{3}{2}$–$2\frac{3}{2}\frac{1}{2}$ and $3\frac{5}{2}\frac{5}{2}$–$2\frac{3}{2}\frac{3}{2}$ are partially blended with $3\frac{5}{2}\frac{7}{2}$–$2\frac{3}{2}\frac{5}{2}$. Assuming equal contributions to integrated intensity.

[d] Using abundance ratios [^{12}C] : [^{13}C] = 65 : 1 and [^{16}O] : [^{18}O] : [^{17}O] = 2695 : 5 : 1.

in particular, can be reproduced by these parameters, and what the implied molecular abundances are.

We use a Monte Carlo code recently developed in Chapter 7 to solve the non-LTE excitation and line transfer in a spherically symmetric envelope with a density and temperature distribution as derived from the dust in §6.3.2. An inner radius of 100 AU is adopted, which does not influence the results. Because of the imperfect coupling between gas and dust, and the cooling of the gas through line radiation, the gas kinetic temperature will be lower than the dust temperature. We adopt $T_{\rm kin} = 0.8 \times T_{\rm dust}$, based on self-consistent models by Ceccarelli et al. (1996) and Doty & Neufeld (1997), but the exact value is not critical. The core is assumed to be static with a turbulent width of 1.5–2.0 km s^{-1} FWHM throughout. This reproduces the observed FWHM line width of the C^{17}O, C^{18}O, and H^{13}CO$^+$ lines. The effect of neglecting any systemic velocity field, like infall, is to increase the optical depth for material close to the center, thereby decreasing the integrated intensity of lines of ^{12}CO, HCO$^+$, and HCN (cf. Chapter 7).

Table 6.6 compares the observed line intensities with predictions in similar beams for the model parameters derived in §6.3.2. We find that in order not to overproduce the single-dish C^{18}O 2–1 emission, the abundance has to be decreased by a factor of ~ 5 when $T_{\rm kin} < 20$ K, corresponding to freeze-out of CO onto dust grains. The gas temperature falls below this value outside r =2000 AU. This freeze-out also reproduces the observed ratio of C^{18}O 2–1 over C^{17}O 3–2. The latter transition primarily traces material with $T_{\rm kin} \gtrsim 30$ K, and is therefore unaffected by depletion in material with $T_{\rm kin} < 20$ K. If no freezing-out is included, the kinetic temperature has to be lowered

Table 6.6. Comparison between observations and simple envelope model[a]

	SMM 1			SMM 3			SMM 4		
	$\int T_{\rm mb} dV$			$\int T_{\rm mb} dV$			$\int T_{\rm mb} dV$		
Line	obs	mod	$X_{\rm mol}$	obs	mod	$X_{\rm mol}$	obs	mod	$X_{\rm mol}$
^{12}CO 4–3[b]	232	18	$\equiv 1(-4)$	171	41	$\equiv 1(-4)$	149	26	$\equiv 1(-4)$
^{12}CO 6–5[c]	222	13		166	26		135	16	
^{13}CO 1–0[d]	27	42	$\equiv 2(-6)$	12	12	$\equiv 2(-6)$	< 0.8	17	$\equiv 2(-6)$
^{13}CO 2–1[b]	27	17		43	28		43	25	
^{13}CO 3–2[b]	36	16		50	28		46	23	
^{13}CO 6–5[b]	41	7		13	11		9	7	
C^{18}O 1–0[d]	7	21	$\equiv 2(-7)$	< 0.5	5	$\equiv 2(-7)$	4	5	$\equiv 2(-7)$
C^{18}O 2–1[b]	10	8		8	9		11	10	
C^{17}O 3–2[b]	6	4	$\equiv 4(-8)$	3	4	$\equiv 4(-8)$	4	4	$\equiv 4(-8)$
HCO$^+$ 1–0[d]	48	31	$5(-9)$	9	23	$1(-9)$	41	26	$3(-9)$
HCO$^+$ 3–2[b]	33	13		22	16		36	18	
HCO$^+$ 4–3[b]	48	14		20	16		25	17	
H^{13}CO$^+$ 1–0[d]	13	15	$8(-11)$	< 0.4	0.7	$2(-11)$	5	2	$4(-11)$
H^{13}CO$^+$ 3–2[b]	6	4		2	1		3	2	
H^{13}CO$^+$ 4–3[b]	3	5		0.2	2		1	3	
HCN 1–0[d]	22	25	$5(-9)$	33	6	$1(-9)$	31	7	$1(-9)$
HCN 4–3[b]	18	11		10	9		14	8	
H^{13}CN 1–0[d]	5	7	$8(-11)$	< 1	0.2	$2(-11)$	< 0.6	0.2	$2(-11)$
H^{13}CN 4–3[b]	3	3		< 0.8	0.6		< 0.5	0.9	
H_2CO 5_{15}–4_{14}[b]	8	5	$1(-9)$	7	5	$4(-9)$	6	8	$3(-8)$
H_2CO 7_{17}–6_{16}[b]	7	5		< 1.3	5		< 1.6	5	
H_2CO 3_{03}–2_{20}[b]	5	4		5	4		11	10	
H_2CO 3_{22}–2_{21}[b]	2	0.6		2	0.5		3	1	

[a] Envelope model as described in §6.4.3, not including the additional $\sim$ 1% of $\sim$ 100 K material.
[b] In JCMT beam
[b] In CSO beam
[b] After sampling at (u,v) positions of the OVRO date, and averaging over a $5'' \times 5''$ area
Note: Listed intensities are integrated values in K km s^{-1}

to an unrealistic value of $0.5 \times T_{\rm dust}$ to fit the C^{18}O 2–1, which will yield C^{17}O 3–2 emission significantly below the observed intensity.

The listed abundances of HCO$^+$, HCN, and H_2CO have been derived by fitting the model results to the observed single-dish integrated line intensities of H^{13}CO$^+$, H^{13}CN, and H_2CO 3_{03}–2_{02}. Standard isotopic ratios are assumed, as well as an ortho-to-para ratio of 3:1 for H_2CO. Like CO these molecules are assumed to be depleted by a factor of 5 at $T_{\rm kin} < 20$ K. This does not affect the results, since most of the lines used in deriving the abundances trace gas well above this temperature. The derived HCO$^+$, HCN, and H_2CO abundances are $(1–5)\times10^{-9}$, and agree well with previous results of McMullin et al. (1994) for SMM 1, and other class 0 YSOs (e.g., IRAS 16293$-$2422, van Dishoeck et al. 1995). Only toward SMM 4 do we find a much larger H_2CO abundance of 3×10^{-8}

due to the large observed intensity of the H_2CO 3_{03}–2_{02} line, possibly indicating that H_2CO is strongly enhanced in the warm central regions of the envelope.

The single-dish lines of HCO^+, HCN, and H_2CO 5_{15}–4_{14} are reproduced within a factor of 2 by the model. Although only a few percent of the envelope material has a temperature > 50 K, this is sufficient to explain 20% or more of the ^{13}CO 6–5 emission. The remaining ^{13}CO 6–5, and almost all ^{12}CO 4–3 and 6–5 emission, probably originates in the outflow. Fitting these ^{12}CO and ^{13}CO lines requires column densities of 9×10^{21} cm^{-2} toward SMM 1 and 7×10^{20} cm^{-2} toward SMM 3 and 4, assuming a kinetic temperature of 100 K and LTE excitation. This material adds less than 2 K km s^{-1} to the $C^{18}O$ and $C^{17}O$ lines. It seems likely that this warm material is responsible for a significant fraction of the H_2CO emission, since the envelope model cannot satisfactorily fit the 3_{22}–2_{21} and 7_{17}–6_{16} lines. This would decrease the derived H_2CO abundance in the envelopes by a factor of a few.

On the smaller scales of 300–4000 AU sampled by the interferometer, the envelope model predicts line intensities within a factor of 3 of the observed values. To derive these intensities, the model data have been sampled at the same (u, v) positions as the observations. In §§6.4.1.1–6.4.1.4 masses were derived from the ^{13}CO and $C^{18}O$ lines observed with OVRO which were 30 times smaller than the values derived in §6.3.2 from the dust emission. The results presented in Table 6.6 show that such low fractions of recovered emission are fully consistent with the obtained envelope parameters, since almost all predicted line fluxes agree within a factor of 3 with the observations. This good agreement indicates that there are no strong abundance changes on small scales. Only toward SMM 3 is the $C^{18}O$ emission in the OVRO beam overestimated by a factor of 10. It should be noted that this source has the lowest envelope mass, and the derived density structure is somewhat uncertain. The failure to reproduce the $C^{18}O$ emission suggests that its envelope structure deviates significantly from of $p = 2$ power-law on small scales of 1000–3000 AU. For all sources, a more realistic treatment of the velocity field and possible variations from spherical symmetry are required before reliable abundance constraints can be derived. The inferred additional column of warm gas toward SMM 1 could contribute significantly to the interferometric flux of ^{13}CO, HCO^+, and HCN if unresolved and not obscured by foreground envelope material. This material is not expected to contribute more than 10% of the observed emission in lines of other species, or any line toward SMM 3 and 4, owing to the lower column density.

6.5 Discussion

6.5.1 Envelopes and disks around class 0 and I YSOs

The inferred density structure for the envelopes around the Serpens YSOs as a radial power law with a slope of -2.0 ± 0.5 agrees well with previous results for class 0 YSOs and theoretical expectations. Zhou et al. (1993) and Choi et al. (1995) find that molecular line profiles observed toward the class 0 YSOs B335 and IRAS 16293−2422 can be accurately reproduced using the inside-out collapse model of Shu (1997). This model predicts density power-law indices between −1 and −2. Recent millimeter-continuum mapping observations of dense cores with and without embedded stars have shown that the former have density distribution with $\rho \propto r^{-p}$ with $p \approx 2$, while the latter have a significantly flatter distribution in the inner few thousand AU (Ward-Thompson et al. 1994; André, Ward-Thompson, & Motte 1996; and Motte, André, & Neri 1998). Our interferometric millimeter-continuum observations directly trace these size scales, and confirm that the envelopes around class 0 YSOs are strongly centrally concentrated.

In chapters 2 and 3 (Hogerheijde et al. 1997a, 1998a), we studied a sample of nine class I YSOs in Taurus through a data set which is very similar to that presented here. The millimeter continuum emission toward at least two-thirds of these class I sources is dominated by an unresolved component, presumably a disk, carrying 30%–75% of the total 1 mm flux. The point-source flux required in §6.3.2 to fit the interferometer continuum observations of the SMM 1, 3, and 4 amounts to only 20%–30% of the total 1.1 mm flux. This indicates that any circumstellar disk makes a much smaller relative contribution to the total flux of class 0 sources than for class I objects, especially since a sizeable fraction of this point-source emission may also be attributable to the warm, inner 100 AU of the envelope. No limits on disk masses can therefore be obtained for the Serpens class 0 sources from the present data.

Significant, resolved emission around the Taurus class I sources was only detected toward L1551 IRS 5 and L1527 IRS. The visibility fluxes of the latter source, which is sometimes referred to as a class 0 source, closely resemble those of the Serpens class 0 YSOs, but its total envelope mass is only 0.03 $M_\odot$, and the signal-to-noise is insufficient to fit an envelope model as in §6.3.2. The envelopes around all Taurus class I sources, including L1527 IRS, contain less than 50% of the estimated stellar mass, consistent with their larger age. Because of their lower masses, these envelopes of class I sources are much better traced by molecular lines than by continuum emission. HCO^+ 1–0, 3–2, and 4–3 single-dish observations of the Taurus class I sources showed that their envelopes are well described by a power-law density structure, similar to that derived here for the Serpens class 0 objects. From the integrated intensities observed in Chapter 2 (Hogerheijde et al. 1997a), the power-law slope is constrained to -1 to -3. These values are consistent with predicted values of -1 to -2 for a collapsing cloud (Shu 1977). By including the complete observed line profile in the model fit, much more accurate constraints on age and envelope density structure can be obtained (cf. Zhou 1992, 1995; Zhou et al. 1993; Walker, Narayanan, & Boss 1994; Choi et al. 1995; Chapter 3, Hogerheijde et al. 1998a).

The Serpens YSOs studied in this chapter have formed within a projected distance of 25,000 AU of each other. The detection of widespread emission from moderate J lines of CO with broad profiles (White et al. 1995) indicates that material throughout the Serpens cloud is influenced by the outflows. It is therefore remarkable that the 16,000 AU diameter envelopes surrounding the YSOs are so well fit by the density structure predicted for the formation of an isolated star (Shu 1977; §6.3.2). This suggests that the influence of the outflows on the cloud structure is largely confined to lower density material, leaving the dense cores mostly unaffected. Alternatively, their envelopes may reflect the original, relatively isolated state if all three YSOs have formed within an interval shorter than the dynamic time scale of the outflows of ~ 8000 yr as estimated from the ^{12}CO 2–1 data of White et al. (1995). However, the projected location of SMM 3 at the edge of the outflow driven by SMM 4, and small age suggested by the small opening angle of SMM 3's outflow as traced by HCN 1–0, may indicate induced star formation. Single-dish mapping of the entire cloud on $10''$–$15''$ scales, well matched to the interferometer observations, are required to further investigate the influence of star formation on the cloud structure. Such observations may also shed further light on the nature of the apparently starless core SMM 2.

6.5.2 Molecular abundances in class 0 envelopes

The model results of §6.4.3 indicate that the abundance of CO in the envelopes around the Serpens sources may be decreased by a factor of 5 in region where $T_{\rm kin} < 20$ K. Two very similar class 0 YSOs, NGC 1333 IRAS 4A and B, are investigated by Blake et al. (1995), who present an extensive molecular line survey. Submillimeter observations indicate envelope masses of 9 and 4 $M_\odot$ in a $20''$ beam, adopting a distance of 350 pc, comparable to those of the Serpens sources. The dust temperatures of $\sim$ 30 K are also very similar. Based on a detailed excitation analysis, Blake et al. conclude that the abundances in the quiescent gas are close to dark cloud values with respect to CO, but that all molecules are depleted by a factor of 10–20 when using the dust emission as a standard. For the Serpens sources we find in §6.4.3 that CO is likely depleted by a factor of 5 in material with $T_{\rm kin} < 20$ K, based on the envelope model inferred in §6.3.2 from the dust emission. The dust emissivity at 1 mm adopted in this chapter is a factor of $\sim$ 2 smaller than that used by Blake et al., further increasing the difference between the inferred depletions by the same factor to almost an order of magnitude. The envelopes of these sources have otherwise very similar conditions, and the large difference in inferred levels of depletion suggests that the quiescent evolutionary phase characterized by heavily depleted abundances may be relatively short-lived, and highlights the difficulty in deriving and interpreting molecular depletion (cf. Mundy & McMullin 1997).

The line profile shapes toward NGC 1333 IRAS 4A and B resemble those of the Serpens sources. Blake et al. conclude that the HCN 4–3 profile, which is significantly broader than, e.g., HCO^+ 4–3, indicates that HCN may be enhanced in the outflow. Our HCN 4–3 spectra show this same trend. In the interferometer beam, $H^{13}CN$ 1–0 peaks toward the northern outflow lobe of SMM 3, supporting the interpretation of larger abundances in the outflow. Enhanced abundances of volatile species like H_2CO and CH_3OH toward NGC 1333 IRAS 4A and B are attributed by Blake et al. to grain-grain collisions in the velocity-shear zones surrounding the outflow. These collisions heat the dust grains transiently and evaporate the ice mantles. Possibly, the dynamic interaction of the outflow with the surrounding envelope could explain the bright emission of HCO^+ and HCN outlining the walls of the outflow cavities of the Serpens sources and other YSOs.

6.6 Summary

In this chapter we investigate continuum and molecular line emission from four protostellar candidates in the Serpens Molecular Cloud: SMM 1 = FIRS 1, SMM 2, SMM 3, and SMM 4. We confirm the nature of SMM 1, 3, and 4 as deeply embedded, class 0

YSOs with more than 50% of the total mass still in a circumstellar envelope. The density in these envelopes is well described by a power-law with slope -2.0 ± 0.5. This agrees with theoretical predictions for an isolated cloud core, even though the SMM 1, 3, and 4 are in close proximity of each other, and outflowing gas permeates the whole Serpens core. The characteristics of, at least, the early phases of star formation therefore do not seem to be very different between isolated and more clustered environments. Large degrees of molecular depletion by freezing-out of molecules onto grains have been inferred for some class 0 YSOs, but the modest levels of depletion found toward the Serpens sources suggests this phase may be short-lived. SMM 2 is most likely a warm cloud condensation without a central object since it shows no compact continuum or molecular line emission. The main conclusions of this chapter can be summarized as follows:

1. The interferometric observations of SMM 1, 3, and 4 in 3.4–1.4 mm dust continuum emission are excellent tools to derive the structure of the envelopes surrounding these class 0 sources. The sources are characterized by intense, resolved ($> 2'' = 800$ AU) emission which can be described by a density distribution that follows a radial power law with index -2.0 ± 0.5. Such a density distribution agrees well with model predictions for the earliest phases of protostellar collapse (e.g., Shu 1977). The temperature distribution is based on self-consistent model results, and fits to the millimeter and far-infrared SED. At a representative radius of 1000 AU, dust temperatures of 27 K (SMM 1), 24 K (SMM 3), and 20 K (SMM 4) are found. The mass contained within the envelopes is constrained to 8.7 $M_\odot$ for SMM 1, 3.0 $M_\odot$ for SMM 3, and 5.3 $M_\odot$ for SMM 4. To fit the flux on long baselines, a point source with 20%–30% of the total flux is required, corresponding to emission originating from radii < 100 AU. Observations at higher spatial resolution are required to investigate how much of this flux is due to a circumstellar disk and how much to the dense inner 100 AU of the power-law envelope.

2. The aperture-synthesis molecular line observations reveal $5''$–$10''$ (2000–4000 AU) diameter cores around SMM 1, 3, and 4 in $C^{18}O$, ^{13}CO, $H^{13}CO^+$, and $H^{13}CN$. The HCO^+, HCN, and N_2H^+ emission traces the walls of the outflow cavities, while SiO and SO emission originates from material shocked by the outflows.

3. Single-dish lines, tracing higher excitation material, show broad outflow wings and deep, narrow self-absorption features, in addition to Gaussian line cores of 2–3 km s^{-1} FWHM. The presence of ^{12}CO 4–3 and 6–5, ^{13}CO 6–5, and several H_2CO lines indicates the presence of gas with a kinetic temperature of > 100 K. This warm material amounts to less than 1% of the total mass in the envelope.

4. Monte Carlo calculations of the molecular excitation and line transfer show that the envelope model derived from the dust emission can successfully reproduce the observed single-dish and interferometric line intensities, except for the $< 1\%$ of warm material traced in the ^{12}CO, ^{13}CO 6–5, and some of the H_2CO lines. The CO abundance appears decreased by a factor of 5 in the regions of the envelope where the gas temperature is 20 K or less ($r > 2000$ AU) owing to freezing-out onto grains. The derived HCO^+ and HCN abundances on single-dish scales of ~ 6000 AU are (1–5)$\times 10^{-9}$. For H_2CO (1–30)$\times 10^{-9}$ is found, which may be enhanced in the warm central region of the envelope. The model predicts interferometric line fluxes which are within a factor of 3 of the observed values, indicating that there are no large abundance variations on scales of

300–4000 AU. However, a more realistic treatment of the velocity field and possible deviations from spherical symmetry have to be included before firmer limits can be placed on the abundances.

Acknowledgments The authors are grateful to the staffs of the JCMT, CSO, and OVRO telescopes for their assistance. Remo Tilanus and Fred Baas are thanked for carrying out part of the JCMT observations. Lee Mundy and Huib Jan van Langevelde are acknowledged for useful discussions. Floris van der Tak kindly assisted in deriving the self-consistent temperature structure of the envelopes. M. R. H. is indebted to the Caltech Divisions of Geological and Planetary Sciences and Mathematics, Physics and Astronomy, and the Owens Valley Radio Observatory for hospitality, and to the Netherlands Organization for Scientific Research (NWO) and the Leids Kerkhoven-Bosscha Fonds for travel support. Research in Astrochemistry in Leiden is supported by NWO/NFRA through grant no. 781–76–015. G. A. B. gratefully acknowledges support provided by NASA grants NAG5–4383 and NAG5–3733.